LOOKING INTO THE FIREBALL: ROTSE-III AND *SWIFT* OBSERVATIONS OF EARLY GAMMA-RAY BURST AFTERGLOWS

E. S. RYKOFF[1,19], F. AHARONIAN[2], C. W. AKERLOF[3], M. C. B. ASHLEY[4], S. D. BARTHELMY[5], H. A. FLEWELLING[3], N. GEHRELS[5], E. GÖĞÜŞ[6], T. GÜVER[7], Ü. KIZILOĞLU[8], H. A. KRIMM[5,9], T. A. MCKAY[3], M. ÖZEL[10], A. PHILLIPS[4], R. M. QUIMBY[11], G. ROWELL[12], W. RUJOPAKARN[13], B. E. SCHAEFER[14], D. A. SMITH[15], W. T. VESTRAND[16], J. C. WHEELER[17], J. WREN[16], F. YUAN[3], AND S. A. YOST[18]

[1] Physics Department, University of California at Santa Barbara, 2233B Broida Hall, Santa Barbara, CA 93106, USA; erykoff@physics.ucsb.edu
[2] Max-Planck-Institut für Kernphysik, Saupfercheckweg 1, 69117 Heidelberg, Germany
[3] Department of Physics, University of Michigan, Ann Arbor, MI 48109, USA
[4] School of Physics, Department of Astrophysics and Optics, University of New South Wales, Sydney, NSW 2052, Australia
[5] NASA Goddard Space Flight Center, Laboratory for High Energy Astrophysics, Greenbelt, MD 20771, USA
[6] Faculty of Engineering & Sciences, Sabancı University, Orhanlı-Tuzla, 34956 İstanbul, Turkey
[7] Department of Astronomy, University of Arizona, Tucson, AZ 85721, USA
[8] Middle East Technical University, 06531 Ankara, Turkey
[9] Universities Space Research Association, 10227 Wincopin Circle, Suite 212, Columbia, MD 21044, USA
[10] Çağ Üniversitesi, Faculty of Arts and Sciences, Yenice-Tarsus/Mersin, Turkey
[11] Division of Physics, Mathematics and Astronomy, California Institute of Technology, Pasadena, CA 91125, USA
[12] School of Chemistry & Physics, University of Adelaide, Adelaide 5005, Australia
[13] Steward Observatory, University of Arizona, 933 North Cherry Avenue, Tucson, AZ 85721, USA
[14] Department of Physics and Astronomy, Louisiana State University, Baton Rouge, LA 70803, USA
[15] Guilford College, Greensboro, NC 27410, USA
[16] Los Alamos National Laboratory, NIS-2 MS D436, Los Alamos, NM 87545, USA
[17] Department of Astronomy, University of Texas, Austin, TX 78712, USA
[18] Department of Physics, College of St. Benedict/St. John's University, Collegeville, MN 56321, USA

ABSTRACT

We report on a complete set of early optical afterglows of gamma-ray bursts (GRBs) obtained with the Robotic Optical Transient Search Experiment (ROTSE-III) telescope network from 2005 March through 2007 June. This set is comprised of 12 afterglows with early optical and *Swift*/X-Ray Telescope observations, with a median ROTSE-III response time of 45 s after the start of γ-ray emission (8 s after the GCN notice time). These afterglows span 4 orders of magnitude in optical luminosity, and the contemporaneous X-ray detections allow multi-wavelength spectral analysis. Excluding X-ray flares, the broadband synchrotron spectra show that the optical and X-ray emission originate in a common region, consistent with predictions of the external forward shock in the fireball model. However, the fireball model is inadequate to predict the temporal decay indices of the early afterglows, even after accounting for possible long-duration continuous energy injection. We find that the optical afterglow is a clean tracer of the forward shock, and we use the peak time of the forward shock to estimate the initial bulk Lorentz factor of the GRB outflow, and find $100 \lesssim \Gamma_0 \lesssim 1000$, consistent with expectations.

Key word: gamma rays: bursts

Online-only material: color figures, machine-readable table

1. INTRODUCTION

The launch of the *Swift Gamma-Ray Burst Explorer* (Gehrels et al. 2004) has brought considerable advancement to the study of gamma-ray bursts (GRBs). The rapid identification of GRBs by *Swift* Burst Alert Telescope (BAT; Barthelmy et al. 2005), combined with its excellent position resolution, has allowed robotic automated ground-based telescopes such as ROTSE-III (Akerlof et al. 2003), TAROT (Klotz et al. 2009), RAPTOR (Vestrand et al. 2004), and REM (Zerbi et al. 2001) to respond promptly to GRBs with regularity, often taking images contemporaneously with significant γ-ray emission. Furthermore, the *Swift* X-Ray Telescope (XRT; Hill et al. 2004) spectrometer provides soft X-ray coverage of the tail of the prompt event and the early afterglow. Combined, these observations provide an unprecedented view into the fireball of the early GRB afterglow.

The "fireball model" of GRB emission (for a review, see Piran 2005) has been successful in predicting the gross behavior of the late burst afterglow. However, there are several inconsistencies between observations and modeling for individual bursts, especially at the earliest times. Most early X-ray afterglows have a portion where the decay is significantly slower than predicted by the fireball model, and this has been interpreted as evidence for long-duration steady energy injection into the forward shock (e.g., Nousek et al. 2006; Zhang et al. 2006). However, the cessation of early energy injection would be expected to produce an achromatic light curve break, which is not generally observed (e.g., Panaitescu et al. 2006; Fan & Piran 2006), although interpretation of X-ray breaks is not always straightforward (Racusin et al. 2009). Observations of individual bursts (e.g., Akerlof et al. 1999; Smith et al. 2003; Rykoff et al. 2004, 2006b; Woźniak et al. 2005; Quimby et al. 2006; Vestrand et al. 2006; Romano et al. 2006; Molinari et al. 2007; Schady et al. 2007) have been interpreted in the context of various models. It is clear that for most early afterglows the "closure relationships" (e.g., Granot & Sari 2002), which compare the spectral index of the synchrotron emission to the temporal decay

---

[19] TABASGO Fellow.

index, are often inconsistent with the fireball model for individual bursts.

Early optical observations can also provide insight into the nature of the fireball, especially by probing the onset of the afterglow, while the early X-ray emission is often dominated by the tail end of the prompt burst emission. However, very early optical detections have been difficult to obtain. The first optical flash observed contemporaneously from a GRB was from GRB 990123 (Akerlof et al. 1999). The ninth magnitude optical flash was not correlated with the high-energy γ-ray emission, and its temporal structure was consistent with reverse shock emission. However, the optical temporal sampling of the light curve was very limited, which made detailed analysis impossible. Other results from optical follow-up to BATSE bursts have shown that these bright optical flashes are rare, but contemporaneous optical detections of large numbers of bursts have not been possible until the *Swift* era. The connection between the prompt optical and γ-ray emission is still not clear. Although GRB 041219a (Vestrand et al. 2005) and GRB 050820a (Vestrand et al. 2006) appear to have a correlation between these two components, this has not been seen for other bursts such as GRB 050401 (Rykoff et al. 2005c). Yost et al. (2007a) have conducted a census of Robotic Optical Transient Search Experiment (ROTSE-III) detections and deep non-detections of prompt optical counterparts, and have not observed a strong correlation between the prompt optical and γ-ray emission for these bursts.

Although connecting the high-energy γ-ray emission with contemporaneous optical emission can be instructive, this requires a large extrapolation, from 10^{17} Hz to 10^{14} Hz. To study the full transition from the prompt emission of the internal shock to the external forward shock, we require more complete wavelength coverage. The XRT instrument is ideal to help bridge the gap between the optical and γ-ray bands. The X-ray band is much less affected by Galactic and host absorption than UV or optical, yet the soft X-rays provide a useful probe of the local equivalent hydrogen column density. Furthermore, the sensitivity of the XRT allows monitoring of the high-energy afterglow spectrum for tens of thousands of seconds. However, the early X-ray afterglow often contains flaring activity (Burrows et al. 2007) that appear to originate in late internal shocks (e.g., Fan & Wei 2005; Burrows et al. 2005; Lazzati & Perna 2007; Krimm et al. 2007; Racusin et al. 2009). Thus, when it is bright enough to be detected at the early time, the optical emission might be more of a "clean" tracer of the external shock (e.g., Molinari et al. 2007).

The ROTSE-III array is a worldwide network of 0.45 m robotic, automated telescopes, built for fast ($\sim$6 s) responses to GRB triggers from satellites such as *Swift*. With four sites around the globe at Siding Spring Observatory, Australia; McDonald Observatory, Texas; the H.E.S.S. site, Namibia; and the Turkish National Observatory, Turkey, a ROTSE-III telescope is often ready for a rapid response. The ROTSE-III network commenced regularly responding to GRB triggers from *HETE-II* (Vanderspek et al. 1999) in 2003 (Smith et al. 2003). After the launch of *Swift* in late 2004, ROTSE-III began to respond to a significant number of rapidly and well localized GRBs. For $\sim$30% of *Swift* GRB triggers, a ROTSE-III telescope is open in good weather and dark skies, and is able to respond in less than 1000 s. We thus have a unique set of early GRB afterglow light curves that are uniformly sampled. We note that only a fraction ($\sim$50%) of the bursts that are observed by ROTSE-III are detected (Yost et al. 2007a), and thus ROTSE-III

is only able to probe the brighter afterglows. When the broadband open-filter ROTSE-III data are studied in conjunction with early XRT observations, we can gain a deeper understanding of the emission mechanisms of the early afterglow and its onset.

We have taken a complete set of 12 ROTSE-III afterglow light curves observed between 2005 March and 2007 June for which we have contemporary XRT data. These bursts are described in Section 2. These are a complete census of ROTSE-III optical afterglows in this time period with early ($<$500 s) optical observations; XRT observations within $\sim$1000 s; and more than three significant optical detections. These selection criteria excludes a few bursts with only marginal ROTSE-III detections. This collection of bursts have a median response time of 45 s after the start of γ-ray emission (8 s after the GCN notice time), providing a unique look at the earliest phases of the optical afterglow. For eight of these bursts, the ROTSE-III photometry is being reported here for the first time; for the remainder, the afterglow data have been published previously but have been re-analyzed here.

By studying these early afterglows as a set, we can discover the commonalities as well as the differences. Specifically, we can determine if the spectral and temporal evolution of these afterglows is consistent with the fireball model and a common emission mechanism. For example, reverse shock emission has been postulated as the source of the prompt optical flash of GRB 990123 (Sari & Piran 1999a) and GRB 021004 (Fox et al. 2003; Kobayashi & Zhang 2003), but has not been observed in most early afterglows (e.g., Yost et al. 2007a; Melandri et al. 2008; Klotz et al. 2009). By comparing the early optical and X-ray emission, we can also determine if the shallow decay typically observed in X-ray afterglows is consistent with continuous energy injection into the forward shock. We can also study which afterglow behaviors are part of a continuous distribution, and if any bursts appear to be true outliers. Finally, we can use the unprecedented early optical coverage of many bursts to probe the onset of the afterglow. This can provide constraints on the bulk Lorentz factor of the outflowing material (e.g., Molinari et al. 2007). In similar vein, an analysis of 24 optical afterglows detected within 10 minutes of the burst event was performed on GRB detections from the Liverpool and Faulkes Telescopes (Melandri et al. 2008). They find a wide range of early afterglow behavior, and several afterglows that appear inconsistent with the fireball model.

In Section 2, we summarize the ROTSE-III observations used in this paper. Section 3 describes the data reduction of the ROTSE-III and *Swift* data. In Section 4, we present the qualitative features of the multi-wavelength light curves for the 12 bursts. Section 5 compares the optical flux to the X-ray spectra for the bursts. Section 6 describes quantitatively the temporal evolution of these early afterglows, and Section 7 discusses the large diversity of optical rise times in the context of the fireball model. Finally, we summarize our results and compare them to other recent work in Section 8.

2. OBSERVATIONS

The ROTSE-III array is a worldwide network of 0.45 m robotic, automated telescopes, built for fast ($\sim$6 s) response to GRB triggers from satellites such as *Swift*. They have wide ($1°.85 \times 1°.85$) fields of view imaged onto Marconi 2048×2048 back-illuminated thinned CCDs, and operate without filters. The ROTSE-III systems are described in detail in Akerlof et al. (2003).

Table 1
Summary of GRBs and ROTSE-III Responses

GRB	Trigger Number	t_0[a] (UT)	Position[b] α (J2000)	δ (J2000)	T_{90}[c] (s)	XRT Response[d] (s)	ROTSE Tel.	Response[e] (s)	Peak (mag)	z[f]
050319	111622	09:29:01.44	$10^h16^m47^s.9$	$+43°32'54''.5$	152.5	251	IIIb	164.1	16.0	3.24
050401	113130	14:20:15	$16^h31^m28^s.8$	$+02°11'14''.2$	33.3	150	IIIa	33.2	15.8	2.9
050525a	130088	00:02:53	$18^h32^m32^s.6$	$+26°20'23''.5$	8.8	125	IIIc	363.4	15.0	0.606
							IIId	2348.1		
050801	148522	18:28:02.1	$13^h36^m35^s.4$	$-21°55'42''.0$	19.4	70.5	IIIc	21.8	14.8	1.6
050922c	156467	19:55:50.4	$21^h09^m33^s.1$	$-08°45'29''.8$	4.5	108	IIId	172.4	14.6	2.198
051109a	163136	01:12:20	$22^h01^m15^s.3$	$+40°49'23''.3$	37.2	118	IIIb	35.4	15.0	2.35
060111b	176918	20:15:39	$19^h05^m42^s.48$	$+70°22'33''.6$	58.8	79	IIId	32.8	13.1	1.0?
060605	213630	18:15:44	$21^h28^m37^s.3$	$-06°03'30''.6$	79.1	93	IIIa	49.4	15.3	3.78
060729	221755	19:12:29	$06^h21^m31^s.85$	$-62°22'12''.7$	155.3	124	IIIa	64.5	16.6	0.54
060904b	228006	02:31:03	$03^h52^m50^s.5$	$-00°43'30''.9$	172	69	IIIc	19.3	16.5	0.703
061007	232683	10:08:08	$03^h05^m19^s.6$	$-50°30'02''.5$	75.3	80	IIIa	27.2	9.5	1.26
070611	282003	01:57:13.9	$00^h07^m58^s.0$	$-29°45'19''.4$	12.2	3200	IIIc	44.7	18.2	2.04

Notes.

[a] GRB 050319: Quimby et al. (2006); GRB 050401: Rykoff et al. (2005c); GRB 050525a: Band et al. (2005); GRB 050801: Rykoff et al. (2006b); GRB 050922c: Norris et al. (2005); GRB 051109a: Yost et al. (2007b); GRB 060111b: see the text; GRB 060605: Page et al. (2006); GRB 060729: Grupe et al. (2006a); GRB 060904b: Grupe et al. (2006b); GRB 061007: Schady et al. (2006); GRB 070611: Stroh et al. (2007a).

[b] GRB 050319: Quimby et al. (2006); GRB 050401: Rykoff et al. (2005c); GRB 050525a: Rykoff et al. (2005b); Holland et al. (2005); GRB 050801: Rykoff et al. (2006b); GRB 050922c: Rykoff et al. (2005a); Norris et al. (2005); GRB 051109a: Yost et al. (2007b); GRB 060111b: Perri et al. (2006); GRB 060605: Rykoff & Schaefer (2006); Schaefer et al. (2006); Page et al. (2006); GRB 060729: Grupe et al. (2006a); GRB 060904b: Rykoff et al. (2006a); Grupe et al. (2006b); GRB 061007: Rykoff & Rujopakarn (2006); Schady et al. (2006); GRB 070611: Rykoff et al. (2007b); Stroh et al. (2007b).

[c] Estimates of T_{90} in the 15–350 keV band from Sakamoto et al. (2008).

[d] Delay from trigger time to first XRT observation.

[e] Delay from trigger time to first ROTSE observation.

[f] GRB 050319: Fynbo et al. (2005); GRB 050401: Watson et al. (2006); GRB 050525a: Foley et al. (2005); GRB 050801: de Pasquale et al. (2007), see the text; GRB 050922c: Jakobsson et al. (2005); Piranomonte et al. (2005); D'Elia et al. (2005); GRB 051109a: Quimby et al. (2005); GRB 060111b: see the text; GRB 060605: Peterson & Schmidt (2006); Still et al. (2006); Savaglio et al. (2007); GRB 060729: Thoene et al. (2006); GRB 060904b: Fugazza et al. (2006); GRB 061007: Osip et al. (2006); Jakobsson et al. (2006); GRB 070611: Thoene et al. (2007).

In this paper, we present new ROTSE-III photometry that has not previously been published for eight bursts (GRB 050525a, GRB 050922c, GRB 060111b, GRB 060605, GRB 060729, GRB 060904b, GRB 061007, GRB 070611). The remaining four bursts (GRB 050319, GRB 050401, GRB 050801, GRB 051109a) have ROTSE-III data that have been previously published (Quimby et al. 2006; Rykoff et al. 2005c, 2006b; Yost et al. 2007b), and is re-analyzed here as described in Section 3.1. ROTSE-III telescopes obtained the earliest optical imaging for all but two of the afterglows. Furthermore, although most of these afterglows also have UVOT detections, we focus on the ROTSE-III data due to the unique early coverage provided.

Table 1 lists the details of the 12 burst responses. The columns of the table provide: (1) the GRB name; (2) the *Swift* trigger number; (3) t_0, the onset of γ-ray emission; (4) and (5) the coordinates of the optical afterglow (J2000); (6) the T_{90} duration of the burst as determined from BAT in the 15–350 keV band; (7) XRT response time, relative to the start of γ-ray emission in Column 3; (8) ROTSE telescope with the response; (9) ROTSE-III response time, relative to the start of γ-ray emission in Column 3; (10) peak optical magnitude; (11) burst redshift.

For most of the bursts, we use the *Swift*/BAT trigger time as the start time t_0. For three bursts (GRB 050319, GRB 050401, and GRB 060111b), we detect significant γ-ray emission prior to the trigger time, and we have adjusted the start time in Column 3 of Table 1 accordingly. We have performed systematic checks on the determination of t_0, which are described in

Section 3.2. All but two bursts have spectroscopic redshift determinations. For GRB 050801, multi-wavelength optical and NUV observations with UVOT have been used to estimate a photometric redshift of $z \sim 1.6$ (de Pasquale et al. 2007). For GRB 060111b, the detection in the UV constrains the redshift to be $\lesssim 1.5$. We have therefore assumed a fiducial redshift of 1.0 for this burst.

3. DATA REDUCTION

In the interest of uniformity, we have used the same analysis for all of the bursts presented in this paper. The ROTSE-III optical data were processed using the ROTSE photometry package RPHOT as described in Section 3.1. The analyses of the BAT and XRT observations are described in Sections 3.2 and 3.3. The analysis presented in this paper is not intended to be a comprehensive study of the high-energy emission of these bursts. More detailed spectral comparisons of simultaneous ROTSE-III and BAT observations for all ROTSE-III bursts through GRB 061222 are presented in Yost et al. (2007a).

3.1. ROTSE-III

The ROTSE-III images were bias-subtracted and flat-fielded by our automated pipeline (Rykoff 2005). We used SExtractor (Bertin & Arnouts 1996) to perform initial object detection and to determine the centroid positions of the stars. The images are then processed with the RPHOT photometry program (Quimby et al. 2006) which performs relative photometry on magnitudes

Table 2
ROTSE-III C_R Optical Photometry

GRB	Tel.	t_{start} (s)	t_{end} (s)	C_R	$f_{\nu,O}$ (mJy)	$f_{\nu,X}$ (mJy)
050319	IIIb	164.1	169.1	15.97 ± 0.14	1.48 ± 0.19	
		178.5	183.5	16.31 ± 0.19	1.09 ± 0.19	
		192.9	197.9	16.18 ± 0.15	1.22 ± 0.16	
		207.5	212.5	16.31 ± 0.16	1.09 ± 0.16	
		222.1	227.1	16.86 ± 0.29	0.652 ± 0.171	
		236.4	241.4	16.22 ± 0.15	1.17 ± 0.16	
		250.9	270.5	16.67 ± 0.36	0.781 ± 0.262	0.0253 ± 0.0064
		279.7	284.7	16.43 ± 0.18	0.972 ± 0.165	
		294.2	299.2	16.62 ± 0.24	0.816 ± 0.183	0.00961 ± 0.00363
		308.5	328.5	16.89 ± 0.13	0.635 ± 0.079	0.00630 ± 0.00160

Notes. Magnitudes are not corrected for Galactic extinction. Optical flux densities ($f_{\nu,O}$ at 1.93 eV) have been corrected for Galactic extinction and Lyα absorption in the IGM. X-ray flux densities ($f_{\nu,X}$ at 2.77 keV) are corrected for Galactic and host absorption. All times are relative to t_0 given in Table 1.

(This table is available in its entirety in a machine-readable form in the online journal. A portion is shown here for guidance regarding its form and content.)

calculated with the DAOPHOT PSF-fitting photometry package (Stetson 1987). The unfiltered thinned ROTSE-III CCDs have a peak response similar to an *R*-band filter. The magnitude zero point was calculated from the median offset of the fiducial reference stars to the USNO B1.0 *R*-band measurements to produce C_R magnitudes. When the signal-to-noise ratio (S/N) of individual images is too small for detection, images are stacked in sets of 5, 10, or 20 to obtain deeper exposures. When a detection is not possible the 3σ upper limit is quoted, as calculated from the local sky noise in a 1 FWHM aperture.

The optical photometry and coincident X-ray flux measurements (see Section 3.3) are listed in Table 2. All times are relative to t_0, the start of γ-ray emission, as listed in Table 1. We have converted the ROTSE-III magnitudes to flux density (f_ν) and flux by assuming the unfiltered magnitudes are roughly equivalent to the R_C-band system, with $\nu_{eff} = 4.68 \times 10^{14}$ Hz (see, e.g., Rykoff et al. 2005c, 2006b). When converting the photometric measurements reported in Table 2 to flux and flux density, we have corrected for Galactic absorption and extinction due to Lyα absorption in the intergalactic medium (IGM). To correct for Galactic extinction, we used the values of A_R from Schlegel et al. (1998), which are reported in Table 3. For the bursts at a redshift of $z \gtrsim 2.0$, the Lyα absorption cuts into the ROTSE-III bandpass. To correct for this, we follow the method outlined in Ruiz-Velasco et al. (2007). We first assume the spectral energy distribution of the optical afterglow has a power-law form $f_\nu(\nu) \propto \nu^\beta$, with $\beta = -0.75$. This spectrum is folded with the Lyα absorption in the IGM using the model of Meiksin (2005), and then with the ROTSE spectral response. The fraction of flux lost to absorption by the IGM is converted to an equivalent magnitude offset, reported in Table 3. Note that this value is not very sensitive to the assumption of the input spectrum: changing β by ± 0.25 changes the equivalent magnitude offset by $\lesssim 0.05$.

3.2. Swift/*BAT*

The BAT and XRT observations were processed using the packages and tools available in HEASOFT version 6.1.[20] Initial mask-weighting on the raw event files was performed with `batmaskwtevt` using standard quality cuts. Light curves were generated with a fixed S/N of 6.0 in the 15–150 keV energy band with `batbinevt`. To obtain spectral files, we follow the standard BAT analysis from the BAT DIGEST.[21] The tool `batbinevt`

Table 3
Galactic Extinction and IGM Absorption

GRB	z	Δm_{IGM}	A_R
GRB 050319	3.24	0.147	0.029
GRB 050401	2.90	0.07	0.174
GRB 050525a	0.61	0.0	0.254
GRB 050801	1.6	0.0	0.257
GRB 050922c	2.20	0.01	0.276
GRB 051109a	2.35	0.01	0.508
GRB 060111b	1.0?	0.0	0.297
GRB 060605	3.80	0.38	0.132
GRB 060729	0.54	0.0	0.145
GRB 060904b	0.70	0.0	0.463
GRB 061007	1.26	0.0	0.055
GRB 070611	2.04	0.01	0.033

was used to extract a spectral (`pha`) file with the standard 80 channels over the desired time range (see below). The tool `batupdatephakw` was used to update the BAT ray tracing columns in the spectral file to correct for spacecraft slews during the burst. The tool `batphasyserr` was used to calculate the systematic error, and finally `batdrmgen` was used to generate a spectral response (`rsp`) file.

For most bursts, we use the BAT trigger time as the start time of the burst (t_0). This is the start of the time interval in which a rate increase was first seen on board the *Swift* satellite. For three bursts (GRB 050319, GRB 050401, and GRB 060111b; see Section 2) the γ-ray emission is significantly detected prior to t_{trig}, and we have adjusted t_0 accordingly. Using the light curves generated with `batbinevt`, we have confirmed that the quoted values of t_0 can be equivalently defined as the time at which the γ-ray flux was detected with S/N > 6.0, with a typical error of ± 5 s.

For each burst, we calculate the time-averaged spectrum using XSPEC version 11.3.2 (Arnaud 1996). Many of the bursts exhibit significant spectral evolution, generally from hard-to-soft, as is seen for most GRBs (e.g., Piran 2005). For the purposes of this work, however, it is simpler to use the time-averaged spectrum over the duration of the burst to obtain a straightforward conversion from count-rate to flux in the 15–150 keV band. Detailed comparisons of simultaneous BAT and ROTSE-III detections of these bursts are described in Yost et al. (2007a). Each of the BAT spectra was well fit by a simple power law except for GRB 050525a, which was fit by a GRB model (Band et al. 1993). The resulting spectral indices are shown in

Table 4
BAT Spectral Indices

GRB	Fit Time Range (s)	Γ
GRB 050319	0–170	2.09 ± 0.20
GRB 050401	0–50	1.48 ± 0.08
GRB 050525a	−10–20	0.97 ± 0.15[a]
GRB 050801	−10–50	2.06 ± 0.20
GRB 050922c	−2–4	1.33 ± 0.05
GRB 051109a	−10–50	1.51 ± 0.25
GRB 060111b	−10–100	0.90 ± 0.18
GRB 060605	0–25	1.37 ± 0.19
GRB 060729	−5–150	1.82 ± 0.15
GRB 060904b	−10–230	1.72 ± 0.16
GRB 061007	−10–70	1.04 ± 0.03
	70–300	1.75 ± 0.10
GRB 070611	−3–10	1.61 ± 0.27

Note.
[a] The spectrum of GRB 050525a is well fit by a GRB model function, with $E_{pk} = 79 \pm 15$ keV and the high-energy index fixed at -2.5. The quoted value of Γ is the equivalent low-energy index.

Table 4. To display the BAT light curves on the same plots as the XRT light curves, we have extrapolated the BAT spectra to the XRT range (0.3–10 keV) using the average of the time-averaged BAT power-law index and the XRT power-law index.

For one burst, GRB 061007, we performed a slightly different analysis for a better comparison of the BAT light curve to the early XRT light curve. For this burst, the main event was significantly harder ($\Gamma \sim 1.0$) than the long tail that was detected coincident with the X-ray afterglow ($\Gamma \sim 1.8$). Thus, we have split the spectral analysis into two time bins, from $T - T_{trig} < 70$ s and 70 s $< T - T_{trig} < 300$ s. This shows a better representation of the connection of the prompt event to the early afterglow. Most of the other bursts did not display such dramatic evolution in their spectral indices. The other exception is GRB 060111b, although since there are no multi-wavelength observations contemporaneous with the first peak we did not see the need for a special correction.

3.3. Swift/XRT

The XRT observations were processed with a pipeline that is described in Rykoff et al. (2007a). Initial event cleaning was performed with `xrtpipeline` using standard quality cuts, using event grades 0–2 in WT mode (0–12 in PC mode). For the WT mode data, source extraction was performed with `xselect` in a rectangular box 20 pixels wide and 40 pixels long. Background extraction was performed with a box 20 pixels wide and 40 pixels long far from the source region. For the PC mode data, source extraction was performed with a 30 pixel radius circular aperture, and background extraction was performed with an annulus with an inner (outer) radius of 50 (100) pixels.

After event selection, exposure maps were generated with `xrtexpomap` and ancillary response function (`arf`) files with `xrtmkarf`. The latest response files (v008) were used from the CALDB database. All spectra considered in this paper were grouped to require at least 20 counts per bin using the ftool `grppha` to ensure valid results using χ^2 statistical analysis. Spectral fits were made with XSPEC in the 0.3–10 keV range. All of the X-ray flux measurements, unless otherwise noted, are in the 0.3–10 keV range. The uncertainties reported in this work are 90% confidence errors, obtained by allowing all fit parameters to vary simultaneously.

Several of the PC observations were slightly affected by pile-up, especially in the early observations. When observations suffer from pile-up, multiple soft photons can be observed at nearly the same time, and appear as a single hard photon. Pile-up correction was performed using spectral fitting, following the method described in Romano et al. (2006) and Rykoff et al. (2007a).

For the purpose of generating light curves, we have calculated the time-averaged XRT spectra to obtain a conversion from count rate in the 0.3–10 keV band to unabsorbed flux in the 0.3–10 keV band. For each of the bursts except for GRB 060927 (discussed below) we have fit the spectrum with an absorbed power law, using the `wabs` absorption model (Morrison & McCammon 1983). When fitting combined XRT data sets (e.g., WT mode spectra; pile-up corrected PC spectra; and non piled-up PC spectra) we tie the equivalent hydrogen column density (n_H) and photon index across each data set, and allow the normalizations to float between data sets, as the X-ray afterglow varies with time. To generate X-ray light curves, we bin the source events with a fixed 50 counts per time bin before background subtraction. This ensures a roughly equal S/N across the duration of the observation.

The X-ray light curve of GRB 060729 was very bright and the spectral shape was varying quite rapidly. During the WT observations from 150 s to 356 s post-burst, the spectrum is better fit by a soft GRB model function ($E_{pk} = 2.1 \pm 0.5$ keV) with absorption fixed to the Galactic value (Dickey & Lockman 1990) than by an absorbed power law, which would require absorption that is correlated with the intensity. The merits of this fitting function are discussed in detail in Butler & Kocevski (2007).

We also use the X-ray spectra to estimate n_H^z, the equivalent hydrogen column density at the redshift of the burst. We first fit each XRT spectrum with an absorbed power law, to estimate the total equivalent hydrogen column density, n_H^T. If n_H^T is significantly greater (at >90% confidence) than the Galactic n_H^G at the position of the burst (Dickey & Lockman 1990), then we consider the afterglow to have a significant excess in n_H. We then re-fit the spectrum with a new absorption component at the redshift of the GRB, while fixing n_H^G at the Galactic value.

The X-ray spectral indices and n_H values for the 12 bursts in this paper are listed in Table 5. The spectral index, β_X is defined as $\beta_X = 1 - \Gamma$, for the power-law model $f_\nu \propto \nu_X^\beta$. With the exception of the aforementioned GRB 060729, we have confirmed that none of the spectral indices varied significantly across light curve breaks calculated in Section 6.1 and detailed in Table 7. The observed lack of spectral evolution is consistent with a much more detailed review of XRT light curves (Racusin et al. 2009). We note that all of the spectral indices cluster around $\beta_X \sim -1.0$, which we discuss in greater detail below.

4. MULTI-WAVELENGTH LIGHT CURVES

We have assembled multi-wavelength BAT, XRT, and ROTSE-III light curves for the 12 bursts described in Section 2. The BAT analysis is described in Section 3.2, the XRT analysis is described in Section 3.3, and the ROTSE-III analysis is described in Section 3.1. The BAT fluxes, calculated in the 15–150 keV range, have been extrapolated to the XRT 0.3–10 keV band as described above, for an easier comparison. For plotting purposes, all times have been scaled by $(1 + z)$ to account for cosmological time dilation. Note that we do not have a redshift estimate for GRB 060111b, and we have assumed a fiducial redshift of 1.0 as described in Section 2.

Table 5
X-ray Spectral Indices and n_H

GRB	z	Fit Time Range (s) (s)	β_X	$n_H^{G\,a}$ (10^{22} cm^{-2})	$n_H^{T\,b}$ (10^{22} cm^{-2})	$n_H^{z\,c}$ (10^{22} cm^{-2})
GRB 050319	3.24	$219 - 13362$	-0.99 ± 0.16	0.011	< 0.039	
GRB 050401	2.9	$133 - 10000$	-0.99 ± 0.05	0.049	0.137 ± 0.013	1.4 ± 0.2
GRB 050525a	0.606	$128 - 87212$	-0.98 ± 0.06	0.091	0.18 ± 0.05	0.20 ± 0.10
GRB 050801	1.6	$59 - 56602$	-0.9 ± 0.2	0.07	0.06 ± 0.03	
GRB 050922c	2.2	$107 - 69769$	$-1.09^{+0.07}_{-0.04}$	0.057	0.070 ± 0.015	
GRB 051109a	2.35	$119 - 26874$	-1.10 ± 0.10	0.174	0.26 ± 0.03	1.0 ± 0.4
GRB 060111b	1.0	$83 - 70485$	-1.24 ± 0.16	0.069	0.28 ± 0.07	0.8 ± 0.3
GRB 060605	3.80	$88 - 74165$	-1.00 ± 0.07	0.051	0.07 ± 0.04	
GRB 060729	0.54	$130 - 356$	-1.0 ± 0.2^d	0.049		
		$356 - 12256$	-1.17 ± 0.06		0.11 ± 0.02	0.11 ± 0.04
GRB 060904b	0.70	$70 - 40797$	-1.13 ± 0.04	0.111	0.30 ± 0.05	0.49 ± 0.15
GRB 061007	1.26	$82 - 25372$	-0.97 ± 0.02	0.021	0.19 ± 0.03	0.67 ± 0.13
GRB 070611	2.04	$3288 - 45631$	$-0.8^{+0.4}_{-0.5}$	0.013	< 0.15	

Notes.
[a] n_H^G is the Galactic equivalent hydrogen column density from Dickey & Lockman (1990).
[b] n_H^T is the total equivalent hydrogen column density, assuming all the absorption is at $z = 0$.
[c] n_H^z is the host equivalent hydrogen column density, after fixing the $n_H(z = 0) = n_H^G$.
[d] β_X is the low-energy component of a GRB model function, as described in Section 3.3.

Table 6
Power-law Fits to ROTSE-III Data

GRB	Fit t_{start} (s)	Fit t_{stop} (s)	α	t_{break} (s)	χ^2/ν	In Figure 5
GRB 050319	169	5000	-0.89 ± 0.03	n/a	52.4/32	*
GRB 050401	35	241	-0.69 ± 0.18	n/a	3.2/3	*
GRB 050525a	406	10843	-0.31 ± 0.07	4100 ± 350	38.8/19	*
			-1.27 ± 0.16	$\cdots$		*
GRB 050801	22	10000	-0.12 ± 0.01	228 ± 6	116/42	*
			-1.10 ± 0.01	$\cdots$		*
GRB 050922c[a]	174	3630	-0.74 ± 0.02	n/a	46.4/23	
GRB 050922c[b]	174	3630	-1.18 ± 0.14	364^{+109}_{-58}	8.9/21	*
			-0.66 ± 0.03	$\cdots$		*
GRB 051109a	39	13300	-0.65 ± 0.01	n/a	278.5/38	*
GRB 060111b	35.3	179	-2.35 ± 0.10	n/a	8.0/7	*
GRB 060605	74	6317	1.18 ± 0.33	152 ± 25	55.5/48	*
			0.14 ± 0.06	666 ± 32		*
			-1.00 ± 0.03	$\cdots$		*
GRB 060729	306	3016	$0.91^{+0.67}_{-0.49}$	424^{+79}_{-45}	50.4/39	*
			-0.20 ± 0.04	$\cdots$		*
GRB 060904b[a]	1694	6440	-0.44 ± 0.06	n/a	11.5/7	*
GRB 060904b[b]	583	6440	-1.8 ± 0.4	870 ± 80	38.2/21	
			-0.25 ± 0.04	$\cdots$		
GRB 061007	108	14600	-1.66 ± 0.01	n/a	390/78	*
GRB 070611	768	8900	2.1 ± 0.6	2230 ± 200	7.1/8	
			-0.61 ± 0.14	$\cdots$		*

Notes.
[a] Single power-law fit.
[b] Broken power-law fit.

The multi-wavelength light curves are shown in Figures 1–3. The BAT flux values (extrapolated to 0.3–10 keV) are blue triangles; the XRT flux values (0.3–10 keV) are magenta squares, and the ROTSE-III flux values are the red circles. In all cases, the optical flux is below the X-ray flux.

4.1. Qualitative Comparisons

The temporal behavior of the earlier afterglows is, at first glance, quite diverse. For several of the bursts—GRB 050319, GRB 050401, GRB 050525a, GRB 050922c, GRB 051109a, and GRB 060111b—the optical afterglow is already fading by the time of the first ROTSE-III exposure. For some bursts, this is as soon as 10 s after the start of γ-ray emission. Other afterglows are seen to rise more slowly. The optical afterglows of GRB 060605, GRB 060729, GRB 060904b, and GRB 070611 peak several hundred seconds after the start of γ-ray emission. The afterglow of GRB 061007 shows the most dramatic rise, brightening by over a factor of 50 in the optical in less than 5 s. The diversity of rise times and a possible physical origin are discussed in Section 7.

After the initial optical rise, if it is observed, the optical afterglow typically fades as a power law, although substructure
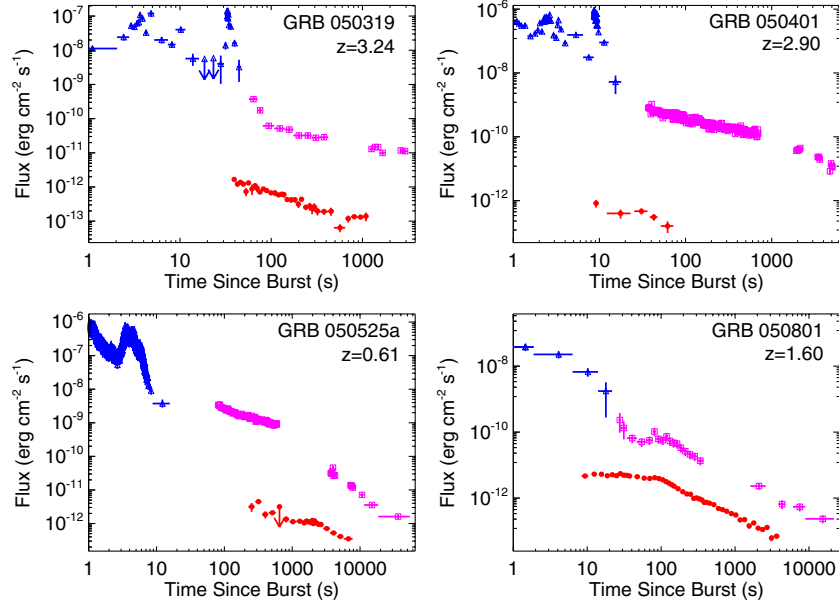
Figure 1. Multi-wavelength light curves for four bursts. The BAT data (blue triangles) have been extrapolated to the X-ray regime as described in Section 3.2. The XRT data are shown with magenta squares, and the ROTSE-III data with red circles. In all cases, the optical flux is below the X-ray flux. The time axis has been corrected for cosmological time dilation. *GRB 050319:* the optical data do not show a deviation from a simple power law, while the X-ray data show the typical steep–flat evolution. *GRB 050401:* neither the optical nor the X-ray data show deviations from simple power laws. *GRB 050525a:* the optical light curve shows a steepening at $\sim$2000 s, while the X-ray light curve shows a slightly more complicated evolution. *GRB 050801:* the optical light curve shows a steepening at $\sim$100 s, and the X-ray light curve shows a very similar morphology.

(A color version of this figure is available in the online journal.)

Table 7
Power-law Fits to XRT Data

GRB	Fit t_{start} (s)	Fit t_{stop} (s)	α	t_{break} (s)	χ^2/ν	In Figure 5
GRB 050319	240	13400	$-4.7^{+0.7}_{-1.1}$	410 ± 30	6.0/11	
			-0.51 ± 0.05	$\cdots$		*
GRB 050401	143	19843	-0.59 ± 0.02	4670 ± 700	197.2/187	*
			-1.37 ± 0.11	$\cdots$		
GRB 050525a[a]	130	58537[c]	-1.25 ± 0.01	n/a	22.2/22	*
GRB 050525a[b]	130	58537	-0.62 ± 0.02	1040 ± 80	95.1/90	*
			-1.71 ± 0.04	$\cdots$		*
GRB 050801	70	50000	$0.04^{+0.5}_{-0.3}$	270^{+70}_{-50}	9.7/17	*
			-1.16 ± 0.05	$\cdots$		*
GRB 050922c[a]	117	65816	-1.17 ± 0.01	n/a	108.4/75	
GRB 050922c[b]	117	65816	-0.74 ± 0.16	289^{+132}_{-61}	74.1/73	*
			-1.23 ± 0.03	$\cdots$		*
GRB 051109a[a]	129	200	-3.1 ± 0.4	n/a	4.2/11	
GRB 051109a[a]	3500	25000	-1.03 ± 0.05	n/a	21.5/36	*
GRB 060111b	93	53058	$-4.64^{+0.8}_{-1.1}$	129 ± 10	20.4/22	*
			-1.09 ± 0.03	$\cdots$		
GRB 060605	102	60000	-1.6 ± 0.6	231^{+153}_{-21}	15.4/18	*
			-0.34 ± 0.08	5770 ± 600		*
			-1.89 ± 0.08	$\cdots$		*
GRB 060729	200	12181	-7.6 ± 0.14	401 ± 11	89/91	
			-1.86 ± 0.6	687 ± 80		*
			0.0 ± 0.03	$\cdots$		*
GRB 060904b[a]	3600	37000	-1.37 ± 0.06	n/a	10.8/14	*
GRB 060904b[b]	89	37000[d]	-0.76 ± 0.04	5600 ± 1500	9.5/14	
			-1.49 ± 0.12	$\cdots$		
GRB 061007	87	24400	-1.68 ± 0.01	n/a	540/322	*
GRB 070611	3392	42000	-0.84 ± 0.23	n/a	5.2/8	*

Notes.

[a] Single power-law fit.

[b] Broken power-law fit.

[c] Excluding the flare from 150 s to 300 s.

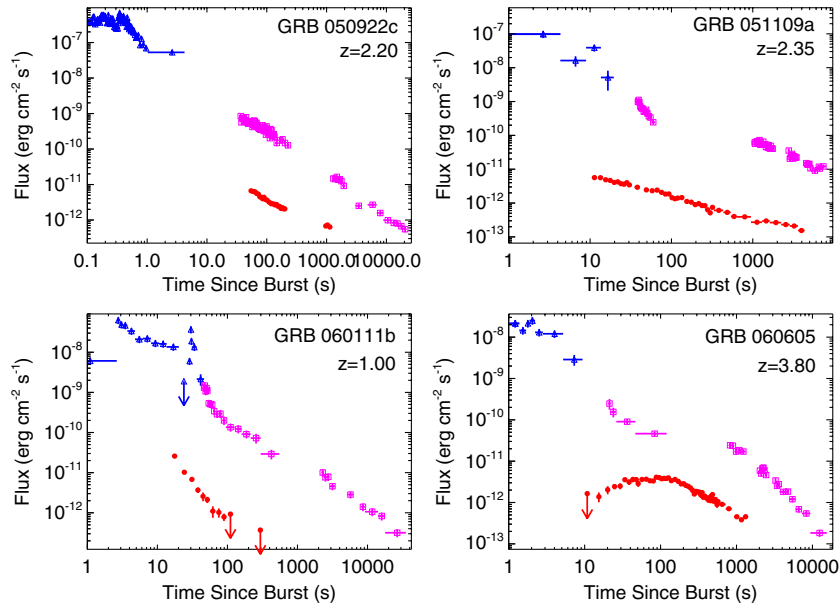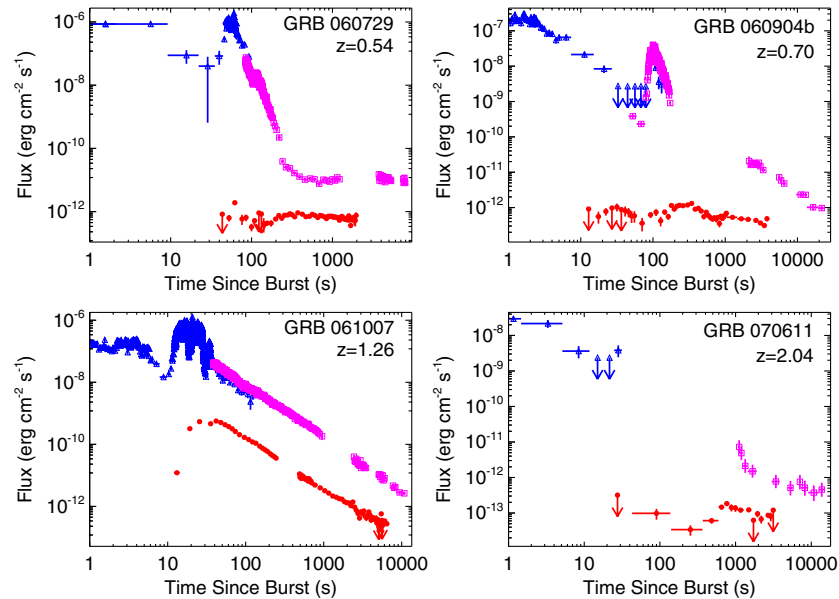[d] Excluding the small flare from 200 s to 1000 s.

Figure 2. Multi-wavelength light curves for four bursts, with the same symbols as Figure 1. The time axis has been corrected for cosmological time dilation. *GRB 050922c:* both the optical and X-ray light curves show a similar morphology, with a simple power-law decline. *GRB 051109a:* the optical light curve follows a simple power law, while the X-ray light curve shows the canonical steep–shallow–steep morphology, although most of the shallow section needs to be inferred from an interpolation over the orbital gap. *GRB 060111b:* the rapidly decaying optical light curve peaks before the second γ-ray peak at ~ 30 s. Note that the time axis has been scaled to an approximate redshift of $z = 1.0$. *GRB 060605:* the optical light curve shows a slow rise and decay, peaking at ~ 100 s, while the contemporaneous X-ray light curve shows the typical steep–shallow–steep canonical form.

(A color version of this figure is available in the online journal.)

Figure 3. Multi-wavelength light curves for four bursts, with the same symbols as Figure 1. The time axis has been corrected for cosmological time dilation. *GRB 060729:* the optical light curve shows two peaks, the first an early flare at ~ 60 s perhaps coincident with one of the γ-ray peaks, and the second around 300–500 s (see Section 7.1). The X-ray light curve shows a typical steep–shallow decay, with a flare around ~ 100 s that is not apparent in the contemporaneous optical light curve. After ~ 300 s, both the X-ray and optical decays are exceptionally shallow, resulting in a very long-lived X-ray afterglow (Grupe et al. 2007, 2009). *GRB 060904b:* the optical light curve is complex for this burst, with short-term variability and an apparent peak at ~ 30 s, followed by a smoother evolution with a peak at ~ 300 s. The X-ray light curve shows a giant flare at ~ 100 s that is not apparent in the contemporaneous optical light curve. *GRB 061007:* the optical light curve shows a dramatic rise, brightening by over a factor of 50 in less than 5 s, followed by two peaks and a steady power-law decline. The γ-ray light curve shows multiple peaks that are not contemporaneous with the optical peaks, followed by a steady decline in the X-rays that tracks the optical decline. *GRB 070611:* there are hints of an early, faint optical peak around ~ 100 s, and a pronounced peak at ~ 700 s. The X-ray light curve is not well sampled due to an orbital break, but there is the hint of the tail of a flare around ~ 1000 s, followed by a shallow decay.

(A color version of this figure is available in the online journal.)

is seen in some bursts. The X-ray afterglow usually follows the "canonical" shape (e.g., Nousek et al. 2006; Zhang et al. 2006; Racusin et al. 2009). This consists of a steep initial decline, a shallow plateau, and another power-law decline. Often there are

X-ray flares superimposed on the canonical afterglow shape, which we observe for GRB 060729 and GRB 060904b. The steep initial decline of the X-ray afterglow has been interpreted as the tail of the prompt emission, possibly caused by high-

latitude burst emission (Kumar & Panaitescu 2000; Liang et al. 2006; Zhang et al. 2007). This interpretation is supported by the fact that the steep early X-ray decline links up with the tail end of the γ-ray emission. Krimm et al. (2007) have also pointed out that for some bursts, later peaks detected by BAT have the same spectral and temporal properties as X-ray flares. Therefore, it may be completely arbitrary to distinguish between the steep initial decline of the X-ray afterglow and an X-ray flare.

At the earliest times, the optical afterglows do not show the same steep decline as the X-ray emission. This suggests that the optical and X-ray emission originate from different regions at the start of the burst: the X-ray emission is dominated by the internal shock emission which produced the GRB itself, and the optical emission is dominated by the onset of the forward external shock. Similarly, we do not observe optical flares contemporaneously with the X-ray flares. This is consistent with the interpretation of the X-ray flares as late internal shock emission (e.g., Fan & Wei 2005; Burrows et al. 2005, 2007; Butler & Kocevski 2007; Lazzati & Perna 2007; Krimm et al. 2007). If, instead, the X-ray flares were caused by density changes in the external medium, one would expect a similar brightening in the optical afterglow which we do not observe.

The shallow plateau that is usually observed in the early X-ray afterglow is significantly less steep than predicted in the standard fireball model. Therefore, it has been interpreted as evidence for long-duration energy injection into the external forward shock (e.g., Nousek et al. 2006). The energy injection model has the advantage of modifying the temporal decay index without altering the synchrotron spectrum. If this hypothesis were correct, we would expect that (a) the decay rate of the contemporaneous optical afterglow is significantly less steep than predicted in the basic fireball model and (b) at the cessation of the energy injection episode there will be an achromatic break observed in both optical and X-ray wavelengths. For the ROTSE-III afterglows, we typically observe that the shallow X-ray decay is accompanied by a shallow optical decay, but this is not always the case, as discussed in Section 6. Additionally, we do not typically observe an achromatic break at the end of the shallow decay phase. This has also been noted by Panaitescu et al. (2006), who showed that the break times associated with the end of continuous energy injection are usually not consistent between the optical and X-ray afterglows. However, the limited temporal sampling of the afterglows described in this paper makes these comparisons challenging.

After the initial optical rise and/or rapid X-ray decay, and excluding X-ray flares, for all the afterglows we observe that the optical and X-ray afterglows display similar trends. As discussed in detail in Section 5, the afterglows that are brighter in optical also tend to be brighter in X-rays. And, as discussed in Section 6, the afterglows that fade rapidly in the optical also fade rapidly in the X-rays (e.g., GRB 061007), while the afterglows that fade slowly in the optical also fade slowly in X-rays (e.g., GRB 060729).

5. BROADBAND SPECTRA

5.1. Fireball Model

In the fireball model, the afterglow is produced by synchrotron emission from shock-accelerated electrons. If the optical and X-ray emission are from the same emission region, there should be a relationship between the spectral and temporal evolution of the optical and X-ray flux density. This relationship depends on the shape of the synchrotron spectrum, especially the location of the various break frequencies. Note that we have adopted the convention that the flux density can be described as a local power law in both time and frequency, such that $f_\nu \propto t^\alpha \nu^\beta$. Here, f_ν is the flux density in units of erg cm^{-2} s^{-1} Hz^{-1}, α is the temporal power-law index, and β is the spectral power-law index. Due to the fact that we observe afterglows both rising and fading, our conventions differ from some other authors in that we explicitly quote the sign of the power-law indices.

Granot & Sari (2002) have compiled a useful list of the various spectral relationships that may be observed during the self-similar evolution of the GRB afterglow in the fireball model. In the more commonly observed "slow cooling" regime, where the cooling frequency, ν_c is above the peak synchrotron frequency, ν_m, then the flux density above the cooling frequency is given by $f_\nu \propto \nu^{-p/2}$, where p is the spectral index of the input electron energies, such that $N(\gamma) \propto \gamma^{-p}$. Below the cooling frequency, $f_\nu \propto \nu^{(1-p)/2}$. It is expected that the X-ray band will always be above ν_c and the optical band will be above or below ν_c depending on the microphysical parameters in the shock, as well as the time elapsed from the start of the burst (e.g., Granot & Sari 2002). For an external shock expanding into a constant density medium, this implies that we may expect a light curve break when ν_c passes through the optical waveband. We note that for the afterglows in this paper, virtually all of the X-ray spectra have a spectral index consistent with $\beta_X \sim -1.0$. This corresponds to an electron spectral index $p \sim 2$, which we have taken as our fiducial value for all the bursts in this paper. The implied electron spectral index is different if we use the temporal decay index α to estimate p, as is discussed in Section 6.2.

If the optical and X-ray emission both originate in the forward external shock, then we can extrapolate the X-ray synchrotron spectrum to the ROTSE-III bandpass to predict the optical flux density. For simplicity, we first neglect optical extinction due to dust in the host galaxy. The maximum optical flux density, $f_{\nu,O}$, corresponding to a given X-ray flux density, $f_{\nu,X}$, will occur when the two bands are in the same synchrotron regime (e.g., the cooling break ν_c is below the optical band). Given the X-ray spectral index of $\beta_X \sim -1.0$, the broadband spectral index between the optical and X-ray band should also be $\beta_{OX} \sim -1.0$. The minimum $f_{\nu,O}$ corresponding to a given $f_{\nu,X}$ will occur when the cooling break ν_c is just below the X-ray band, which yields a relatively flat broadband spectral index, $\beta_{OX} \sim -0.5$.

On the other hand, if the optical and X-ray emission are not from the same region, then we do not expect to observe this simple relationship. For example, if the X-ray flares or steep X-ray decline are from internal shocks caused by late activity of the central engine, then they should not be part of the same synchrotron spectrum as the optical afterglow. Similarly, there may be an optical flash caused by reverse shock emission (Meszaros & Rees 1997; Sari & Piran 1999a, 1999b; Kobayashi 2000), which would instead peak in the NIR/optical/NUV wavelengths. Thus, we expect this optical flash may be *overluminous* compared to an extrapolation of the X-ray emission.

5.2. Optical and X-ray Comparison

We have compared the optical and X-ray flux density ($f_{\nu,O}$ and $f_{\nu,X}$) at multiple epochs for each of the bursts in this paper. For simplicity, we have re-binned the XRT photon data to match the ROTSE-III optical integration times. For each of the optical integrations with overlapping XRT data, we have calculated the
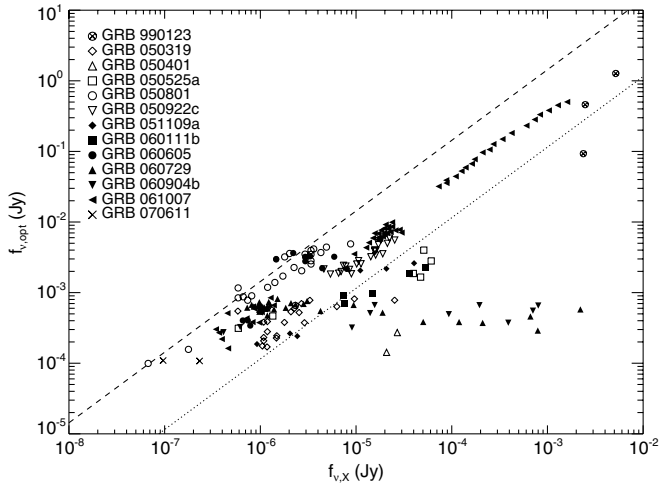
Figure 4. Optical flux density $f_{\nu,O}$ [1.93 eV] vs. X-ray flux density $f_{\nu,X}$ [2.77 keV] for 12 ROTSE-III bursts, as well as GRB 990123. Each individual point in the figure is from a specific burst at a single optical integration. The size of the error bars are typically $\lesssim$10% for the optical data, and $\lesssim$30% for the X-ray data; the bright afterglow of GRB 061007 (leftward triangles) has very large S/N, and the error bars are smaller than the data points. As an afterglow fades, the points will follow a track from the upper right to the lower left. The dashed line shows the prediction from the synchrotron model where the optical and X-ray emission are in the same synchrotron regime with $\beta_{OX} = -1.0$. The dotted line shows the same model with the cooling frequency at 0.3 keV, just below the X-ray band. With the exception of GRB 050401 (open upward triangles), the other observations below the dotted line all correspond to X-ray flares or the tail of the prompt γ-ray emission.

X-ray count rate. We then converted this count rate to $f_{\nu,X}$ at 2.77 keV using the average afterglow spectral parameters used to make the X-ray light curves as described in Section 3.3. We have neglected variations in the X-ray spectral index. These are likely to be quite small for the following two reasons. First, there is no evidence for significant spectral evolution in the X-ray light curve, excluding the initial steep decline and X-ray flares. Second, we have calculated $f_{\nu,X}$ at 2.77 keV, which is the weighted mean of the X-ray emission in the 0.3–10 keV range assuming a spectral index $\beta_X = -1.0$. This ensures that slight changes in the X-ray spectral index from this canonical value will not significantly alter $f_{\nu,X}$. We also note that we have neglected any k-corrections, as these are impossible to calculate for our unfiltered optical data. However, we expect that the spectral index is similar in the optical and X-ray bands. Thus, the sense of the k-correction will be the same for both X-ray and optical data, and may be neglected for the purposes of this analysis.

Figure 4 shows the optical flux density $f_{\nu,O}$ (at 1.93 eV) versus the X-ray flux density $f_{\nu,X}$ (at 2.77 keV). Each individual point in the figure is from a specific burst at a single optical integration. The size of the error bars are $\lesssim$10% for the optical data and $\lesssim$30% for the X-ray data. As an afterglow fades, the points will follow a track from the upper right (bright in X-rays and optical) to the lower left (faint in X-rays and optical). The dashed line shows the prediction from the synchrotron model where the optical and X-ray emission are in the same synchrotron regime ($\nu_c < \nu_{opt} < \nu_X$) with $p = 2.0$ and $\beta_{OX} = -1.0$. The dotted line shows the same model with $\nu_c = 0.3$ keV, just below the X-ray band. Most of the afterglow detections are between the dashed and dotted lines. As $f_{\nu,O}$ and $f_{\nu,X}$ track each other, the spectra are generally consistent with the predictions of the synchrotron model. Furthermore, although there are many optical detections that are "underluminous" compared to the X-

ray detections (those in the lower right corner of the plot), there are no optical detections that are significantly "overluminous," above the dashed line. Each of these points is addressed in turn.

There are two primary reasons for the optical emission to be underluminous in Figure 4. First, there might be significant extinction in the host galaxy. For example, this appears to be the case for GRB 050401 (de Pasquale et al. 2006); we discuss the effects of local extinction in more detail below. Second, in the case of X-ray flares or the steep initial decline, the X-ray flux may be dominated by internal shock emission, and thus is not directly related to the optical flux. This is the most likely explanation for most of the underluminous optical detections in the lower right corner of the figure. GRB 060729 (solid upward triangles) and GRB 060904b (solid downward triangles) each have very bright X-ray flares, and GRB 050525a (empty squares) has a shallow flare. Meanwhile, flaring is not observed in the mostly flat contemporaneous optical afterglows. Excluding the duration where there are obvious X-ray flares, these afterglows have observations that are consistent with the main locus of points that falls within the range expected from a simple synchrotron spectrum. Similarly, other afterglows that appear to be optically underluminous at the earliest times have early X-ray emission dominated by a steep decline (e.g., GRB 051109a, solid diamonds) or prompt emission (e.g., GRB 060111b, solid squares). These are also consistent with a simple broadband spectrum at later times. This is another line of evidence that the steep X-ray decay and X-ray flares are caused by internal shock emission, and are not directly related to the external shock as traced by the optical afterglow.

If the early optical light curve were caused by reverse shock emission (Meszaros & Rees 1997; Sari & Piran 1999a, 1999b; Kobayashi 2000), the optical emission may be *overluminous*. A reverse shock is predicted to cause a prompt optical flash, which will significantly outshine the optical forward shock emission until the reverse shock crosses the ejecta shell. Thus, if the contemporaneous X-ray emission traces the forward shock, the optical emission from the reverse shock will be brighter than an extrapolation of the forward shock synchrotron spectrum. A reverse shock has been hypothesized as the origin of early optical emission for only a few afterglows, notably GRB 990123 (Akerlof et al. 1999). The primary evidence is the temporal evolution of the optical afterglow, which was consistent with predictions: a fast rise followed by a steep ($\alpha_O \sim -2$) decay and a break to a shallower decay ($\alpha_O \sim -1$). However, a similar temporal profile has not been observed for the vast majority of bursts detected since GRB 990123, including the 12 bursts described in this paper. In addition, as shown in Figure 4, none of the bursts in this paper require a separate optical component in excess of the predictions of the external forward shock. The implication that reverse shock emission is not common has been noted by other authors (e.g., Melandri et al. 2008; Gomboc et al. 2009).

We now investigate how the broadband spectral characteristics of the prompt optical flash of GRB 990123, detected by ROTSE-I, compare to the 12 afterglows in this paper. The Wide Field Camera (WFC) on the *BeppoSAX* satellite obtained 2–10 keV X-ray observations of the prompt and early X-ray afterglow of GRB 990123, contemporaneous with the prompt optical flash (Maiorano et al. 2005; Corsi et al. 2005). Corsi et al. (2005) performed spectral fits to the WFC observations during the first three ROTSE-I integration times, including the ninth magnitude optical peak. The X-ray flux densities $f_{\nu,X}$ (2.77 keV) obtained from the WFC observations are directly

comparable to the XRT observations taken at similar times for the ROTSE-III bursts. In Figure 4, we have plotted the ROTSE-I $f_{\nu,\mathrm{O}}$ versus the WFC $f_{\nu,\mathrm{X}}$ with the plotting symbol ⊗. Although the optical flash from GRB 990123 was exceptionally bright in optical, it was also exceptionally bright in X-rays, comparable to GRB 061007. However, unlike the early X-ray afterglows detected for ROTSE-III bursts with a typical spectral index of $\beta_{\mathrm{X}} \sim -1.0$, GRB 990123 had a very hard X-ray spectrum, with a spectral index ranging from $\beta_{\mathrm{X}} \sim 0$ to $\beta_{\mathrm{X}} \sim 0.5$. Therefore, an extrapolation of the X-ray spectrum to the optical regime greatly *underpredicts* the optical flux (see Figure 2 in Corsi et al. 2005). Although the broadband spectral index (β_{OX}) of the prompt optical flash from GRB 990123 does not look quantitatively different from the ROTSE-III detected afterglows, in this case the optical emission is significantly in excess of an extrapolation of the X-ray emission. This extra optical emission component may be reverse shock emission, although other models have been suggested, such as large-angle burst emission (Panaitescu & Kumar 2007).

We note that if the early X-ray observations are dominated by prompt emission, and not the forward shock, then this simple broadband spectral analysis might not hold. This is most likely the case for GRB 060111b, where the rapidly fading optical counterpart was detected *prior* to the second peak of the γ-ray emission, and for GRB 990123, where the spectrum of the early X-ray emission was consistent with the GRB model function measured in the γ-rays. Nevertheless, it is remarkable that none of the optical afterglow detections in this paper, at any time, are significantly brighter than an extrapolation of the X-ray flux using a broadband power-law index $\beta_{\mathrm{OX}} = -1.0$.

The afterglows which have multiple observations that intersect the dashed line in Figure 4 merit particular attention. These are GRB 050801 (empty circles), GRB 060605 (solid circles), and GRB 070611 (×'s). We neglect GRB 061007 (leftward triangles), for which a single late time optical detection at is an anomalous outlier (see Figure 3). The peculiar GRB 050801 had been discussed in detail in Rykoff et al. (2006b). For this afterglow, the optical emission tracks the X-ray emission over more than 2 orders of magnitude in time. In addition, direct extrapolation of the X-ray spectrum predicts $f_{\nu,\mathrm{O}}$, indicating that the optical and X-ray bands are in the same spectral regime. The flux of the two other optical afterglows along the dashed line, GRB 060605 (in the decay phase), and GRB 070611 (in the final ROTSE-III observation), can also be predicted by a direct extrapolation of the X-ray spectrum. We note that the X-ray spectra of these bursts do not show evidence for equivalent neutral hydrogen absorption (n_{H}) in excess of Galactic. Assuming the excess n_{H} is attributable to the local environment, these afterglows will have minimal local extinction. Thus, for a given $f_{\nu,\mathrm{X}}$, these afterglows represent the brightest possible $f_{\nu,\mathrm{O}}$ after correcting for Galactic extinction and IGM absorption. No other optical afterglows are brighter than the simple extrapolation of the X-ray spectrum. This lends further support to our hypothesis that the optical afterglow is dominated by the forward shock, even at the earliest times.

5.3. The Effect of Local Extinction

We now briefly address how local extinction in the host galaxy may cause a given optical afterglow to appear underluminous. GRB 050401 had a remarkably dim afterglow, as well as a very large excess n_{H} in the X-ray spectrum, as shown in Table 5. Although local extinction has been posited as the explanation for the dim afterglow, using the typical Milky Way

(MW) dust-to-gas ratio implies 20–30 mag of extinction, which results in an unphysically bright optical counterpart (de Pasquale et al. 2006). Using well-measured multi-band observations of optical afterglows, Chen et al. (2006) determined that no single extinction law can plausibly explain the optical afterglow light curves, and some bursts are well explained by a "gray" (flat) extinction law, rather than a typical local extinction law. In an expanded analysis, Li et al. (2008) used optical and X-ray afterglows that are in the same synchrotron regime to constrain the extinction law as well as the dust-to-gas ratio for each burst. They do not find a common connection between the optical extinction and X-ray absorption. Similarly, Schady et al. (2008) use UVOT and XRT data and find a wide range in implied dust-to-gas ratio among the afterglows.

With our present single-filter ROTSE-III data, it is not possible to perform a similar analysis to that performed by Li et al. (2008) or Schady et al. (2008). However, we note that a cursory analysis hints that there is a loose relation between n_{H} as determined in the X-ray spectrum and the optical extinction. Three of the afterglows with no excess column density (GRB 050801, GRB 060605, and GRB 070611) have evidence for an absence of local optical extinction. The two afterglows with the largest excess column density (GRB 050401 and GRB 051109a) are consistent with the largest optical extinction. We leave it to future work with multi-band optical data to explore this relationship further.

6. TEMPORAL EVOLUTION

In Section 5, we showed that the early optical afterglow and the early X-ray afterglow generally follow the same track, after excluding the optical rise and X-ray flares. In order to remain on the same track, the optical and X-ray afterglows must be fading at roughly the same rate. In this section, we examine the temporal evolution of the afterglows in more detail.

6.1. Power-law Fits

In order to ascertain the gross temporal profile of the optical and X-ray afterglows in the sample, we perform simple power-law fits to the light curves. These fits are intended to trace the overall time structure and not the short timescale variability that is observed in some of the afterglows.

We fit a broken power law to each of the optical and X-ray afterglows with the following form:

$$f = \left(\frac{t}{t_b}\right)^{\alpha_1} \left[1 + \left(\frac{t}{t_b}\right)^{-s(\alpha_2-\alpha_1)}\right]^{-1/s}, \qquad (1)$$

where f is the flux, t_b is the break time, α_1 and α_2 are the two power laws, and s is a smoothing parameter. We fix $|s| = 10$ to yield a moderately smooth break, where the sign of s is positive when the light curve is steepening and negative with the light curve is getting more shallow. For the majority of light curve breaks, we do not have sufficient temporal coverage or sensitivity to allow us to fit s.

Table 6 shows the results of the power-law fits to the optical light curves. For a few bursts there is ambiguity as to whether a single power-law fit or a broken power-law fit is more appropriate; for completeness, we have presented both fits in the table. For the afterglow of GRB 060605, the fit requires a double-broken power law, which is a natural extension of Equation (1). Table 7 shows the results of the power-law fits to the X-ray light curves, excluding X-ray flares, as noted in the table. We have

also marked when there is ambiguity about the preferred power-law model. We note that some of the χ^2 values for the optical fits, in particular, are quite poor. For example, the optical afterglow of GRB 061007 shows short timescale variability which leads to a very large χ^2 for the fit. The apparently small error bar on the power-law decay index, -1.66 ± 0.01, is driven by the well-determined average decay rate over a long baseline over three decades in time.

The X-ray light curves show the steep–shallow–steep morphology with superimposed flares that has been referred to as the "canonical" X-ray afterglow (Nousek et al. 2006). The optical afterglows do not have such an obvious pattern. For example, we do not always see the rise of the optical afterglow, even when the first ROTSE-III image is taken within seconds after the start of γ-ray emission. The implications of the variety in optical rise time are addressed in Section 7. After the initial rise, some of the optical afterglows decay very slowly (e.g., GRB 050801, $\alpha \sim -0.1$) and some very rapidly (e.g., GRB 061007, $\alpha \sim -1.7$). For most of the optical afterglows where we see an early break, the initial decay is shallower than the later decay, although there are exceptions, such as GRB 050922c (and GRB 990123) which show evidence for an initial shallowing rather than steepening of the light curve.

With the power-law fits, we can also begin to constrain the break times in the optical and X-ray light curves. The typical explanations for a light curve break at the early time are as follows. First, if the fireball is expanding into a constant density medium, when the synchrotron cooling frequency, ν_c, passes through the optical waveband, the decay index should steepen by $\delta\alpha = 0.25$, without a contemporaneous change in the X-ray decay index. Second, cessation of long-duration energy injection should cause an identical steepening of both the optical and X-ray decays, with the magnitude arbitrarily determined by the rate of energy injection. Third, a sudden change in the density of the surrounding medium may cause a chromatic or achromatic break, depending on whether the observed band is above or below ν_c. Finally, if the early optical afterglow is dominated by reverse shock emission, we expect a steep-to-shallow transition in the decay index.

For several *Swift* afterglows, previous work has shown that many light curve breaks are chromatic, and are not observed simultaneously in both the optical and X-ray wavelengths (e.g., Panaitescu et al. 2006; Melandri et al. 2008). These chromatic breaks are difficult to reconcile with the hypothesis that the flat portion of the X-ray afterglow is caused by continuous energy injection: when the energy injection stops, we should see a break in all bands simultaneously. The magnitude of the breaks are also typically not consistent with the passage of ν_c, or with a change in density of the circumburst medium. Using additional optical data, the study by Panaitescu et al. (2006) documents unexplained chromatic breaks in three of the afterglows reported in this paper: GRB 050319, GRB 050401, and GRB 059022c. On the other hand, some afterglows do show achromatic breaks at the early time (e.g., GRB 050801, as described in Rykoff et al. 2006b). Unfortunately, the ROTSE-III telescopes are only able to detect afterglows for a limited duration, and there are orbital gaps inherent in the XRT coverage. Combined, this makes it difficult in this work to shed further light on this important topic. We leave it to future work to integrate the ROTSE-III light curves with later optical observations (as had been done with GRB 050319 and GRB 050401) to better constrain the precise timing of the optical and X-ray breaks.
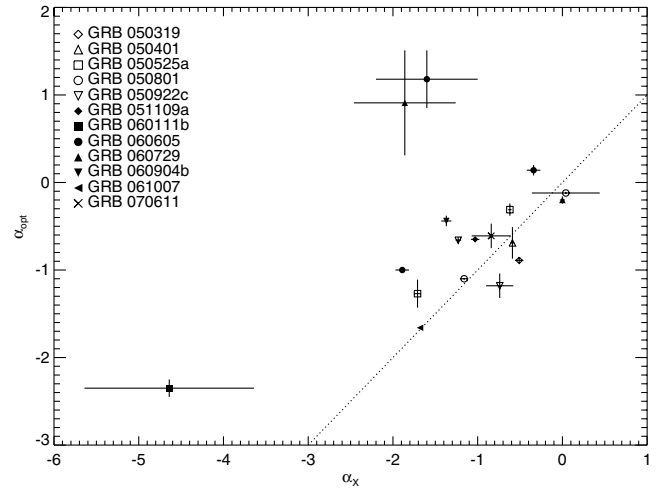

Figure 5. Power-law indices α_O vs. α_X for the 12 ROTSE-III afterglows. The dotted line is the line of equality. In general, the afterglows that fade rapidly in optical fade rapidly in X-rays. The notable exception are the X-ray flares (not shown) and the early optical rise (seen here in early observations of GRB 060605 and GRB 060729). The optical afterglows tend to fade slightly slower than the X-ray afterglows, as predicted if the forward shock is expanding into a constant density medium.

6.2. Optical and X-ray Power-law Comparison

We now investigate the relationship between the optical and X-ray decay rates (α_O and α_X) for each afterglow in the sample. These two quantities are plotted in Figure 5. Each data point represents a single contemporaneous determination of the temporal index α for the ROTSE-III and XRT observations, as denoted by asterisks in Tables 6 and 7. If there were no overlapping observations of a particular temporal segment (e.g., for the optical rise of GRB 061007) then there is no data point on the plot. The dashed line of equality is shown for reference.

Although there is a large scatter, we observe a significant trend in the data indicating that the more rapidly fading X-ray afterglows are correlated with rapidly fading optical afterglows. We note that this tracking behavior was hinted at in the broadband spectral comparison in Figure 4. The three largest outliers are GRB 060111b, where the early optical afterglow is contemporaneous with the tail of the prompt emission observed in X-rays; and the early optical detections of GRB 060605 and GRB 060729, where the optical rise ($\alpha_O > 0$) is paired with a steep decline in the X-rays.

The trend in Figure 5 is most evident in the extreme cases. For example, GRB 050801 (empty circle) and GRB 060729 (solid upward triangle) both have flat decays that are contemporaneous in optical and X-rays. At the lower left of the distribution, GRB 050801 (empty circle), GRB 061007 (leftward triangle), and GRB 050525a (empty square) both show quite steep declines contemporaneously. The rest of the decay indices are all clustered in the middle, with $\alpha_X \sim -1$ and $\alpha_O \sim -0.5$.

The standard fireball model for the afterglow predicts that when the forward shock expands into a constant density (ISM) medium, $\alpha_X \propto t^{(2-3p)/4}$ and $\alpha_O \propto t^{3(1-p)/4}$ when the synchrotron cooling break ν_c is between the optical and X-ray regime (Granot & Sari 2002). Taking our fiducial electron index of $p = 2$ that is implied from the typical X-ray spectral index ($\beta_X \sim -1.0$, with $\beta_X = -p/2$), then we predict $\alpha_X = -1.0$ and $\alpha_O = -0.75$. On the other hand, if the shock is expanding

into a $n \propto 1/r^2$ wind medium, then we predict $\alpha_X = -1.0$ and $\alpha_O = -1.25$. When ν_c is in between the X-ray and optical regime, we expect the optical decay will be slightly slower than the X-ray decay for the ISM case, and we expect the inverse in the wind case. If the X-ray and optical observations sample the same spectral regime (i.e., the cooling break is below the optical regime), we expect $\alpha_X = \alpha_O \sim -1.0$ for both the ISM and wind cases.

It is challenging to shoehorn individual afterglows into this simple toy model. However, in the aggregate they are roughly consistent with the predictions for the forward shock expanding into an ISM medium. First, we observe that the optical and X-ray afterglows typically track each other. Second, the optical decay index α_O is usually *slightly* shallower than the X-ray decay index α_X. Meanwhile, two well-sampled bursts, GRB 050801 and GRB 061007, have the same optical and X-ray decay indices, as also indicated in Figure 4. In these cases, the optical and X-ray observations are consistent with sampling the same spectral regime. Two afterglows, GRB 050319 (empty diamonds) and GRB 060729 (solid upward triangles), decay more rapidly in the optical than the X-rays. This may indicate a different external medium, or it may just represent the large scatter in the α_X–α_O correlation.

Although the difference between the optical and X-ray decay indices is roughly consistent with the predictions of the fireball model, the magnitude of the decay indices are not. Thus, using the X-ray spectral index β_X to infer the electron index p yields different results than using the afterglow decay index α_X or α_O to infer p. These discrepancies are most apparent in the early afterglows of GRB 060729 and GRB 061007. The extraordinarily flat and long-lived afterglow of GRB 060729 has been interpreted as a sign of long-duration energy injection (Grupe et al. 2007), and the X-ray detection almost two years after the burst may also imply a very wide jet (Grupe et al. 2009). On the other side, the remarkably steep decay of GRB 061007 with no indication of a late jet break (or any other break) has been interpreted as evidence for a strongly collimated jet (Schady et al. 2007). We note that in our present analysis there is nothing significantly different between these afterglows at the early times except for the absolute value of the decay indices. Thus, in order to obtain a coherent picture of the early afterglow emission, we must (a) posit a different emission model for each of these bursts individually, or (b) modify the afterglow modeling such that we can accommodate a standard spectral index and a wide range of temporal indices.

We emphasize again that the early optical and X-ray afterglows, after excluding the steep decay phase and X-ray flares, appear to be probing the same emission region. Furthermore, the behavior is roughly consistent with the model for the forward shock. We have assumed that the X-ray spectral index, which is common among the set of afterglows, is a more robust tracer of the underlying electron index. The absolute value of optical and X-ray decay indices shows much more variety, and depends much more strongly on the nature of the circumburst environment and posited long-duration energy injection.

7. OPTICAL RISE TIMES

Due to their rapid response capabilities and sensitivity to typical early afterglows, the ROTSE-III telescopes are uniquely suited to measure the optical rise time of the typical GRB optical counterpart. The optical rise may be tracing the onset of the forward shock (e.g., GRB 060418; Molinari et al. 2007)

or the reverse shock (e.g., GRB 990123; Akerlof et al. 1999), and may be combined with optical emission correlated with the prompt γ-rays from internal shocks (e.g., GRB 050820a; Vestrand et al. 2006). As we have shown, the broadband early afterglow spectra of the bursts described in this paper are all consistent with forward shock emission. In this case, the peak of the optical afterglow can constrain the initial bulk Lorentz factor of the GRB ejecta (Sari & Piran 1999b).

Using the REM telescope, Molinari et al. (2007) detected the optical rise of two early afterglows, GRB 060418 and GRB 060607a, and were able to constrain the initial bulk Lorentz factor of the outflow. Both of these early optical afterglows followed a very smooth evolution in the early rise and fall, with a peak $\sim$150 s after the burst. Furthermore, REM obtained imaging of GRB 060418 with multiple filters, and did not detect significant color evolution at the early time. This is consistent with the predictions for the onset of the forward shock (Sari & Piran 1999b).

The peak time of the optical afterglows of both GRB 060418 and GRB 060607a occurred after the end of the γ-ray emission, such that $t_{pk} > T_{90}$. Therefore, the outflow can be modeled as a "thin shell," the definition of which depends on the relationship between the thickness of the outflowing shell in relation to its Lorentz factor (Sari & Piran 1999b). The "thick shell" case, where the forward shock peak occurs during the γ-ray emission, is more difficult to model. In the thin-shell case, the peak of the optical emission t_{pk} corresponds to the deceleration timescale $t_{dec} \sim R_{dec}/(2c\Gamma_{dec}^2)$, where c is the speed of light, R_{dec} is the deceleration radius, and Γ_{dec} is the bulk Lorentz factor of the fireball at t_{dec}. The initial Lorentz factor Γ_0 is expected to be twice the Lorentz factor at the deceleration time, Γ_{dec} (Meszaros 2006). Assuming that the fireball is expanding in a homogeneous medium with constant particle density n, consistent with the conclusions of Section 6.2, we find

$$\Gamma_0 \sim 2\Gamma_{dec} = 2 \left[\frac{3E_{iso}}{32\pi n m_p c^5 \eta t_{pk,z}^3} \right]^{1/8} \tag{2}$$

$$\approx 560 \left[\frac{E_{iso,52}}{\eta_{0.2} n_0 t_{pk,z,10}^3} \right]^{1/8}, \tag{3}$$

where $E_{iso,52}$ is the isotropic equivalent energy release in γ-rays in units of 10^{52} ergs^{-1}; n is local density and $n = n_0$ cm^{-3}; m_p is the mass of the proton; $\eta = 0.2\eta_{0.2}$ is the radiative efficiency; and $t_{pk,z,10} = t_{pk}/[(1+z)\times 10\,\text{s}]$ is the optical peak-time corrected for cosmological time dilation in units of 10 s.

The calculation of Γ_0 requires an estimation of E_{iso} for each of the GRBs. Unfortunately, BAT only covers a narrow band-pass of 15–150 keV. Some of the bursts listed in this paper have been observed by Konus–Wind, which has a much wider band-pass more suitable for measuring the peak of the γ-ray emission, E_{pk}, and thus allowing an estimation of E_{iso}. As high-energy coverage is limited, Butler et al. (2007) have used a Bayesian analysis using priors from BATSE spectra to estimate E_{pk} and E_{iso} directly from BAT data. As this analysis can be consistently applied to all of the bursts in this paper, we have chosen to use E_{iso} from Butler et al. (2007). For the GRBs with Konus–Wind data, we have confirmed that the estimates of E_{iso} are consistent for each of the methods. Furthermore, the estimation of Γ_0 is only weakly dependent on E_{iso} ($\Gamma_0 \propto E_{iso}^{1/8}$), such that an error of a factor of 2 in E_{iso} will only shift Γ_0 by $\sim$10%.

Table 8
Optical Peak Fits

GRB	$t_{start}(s)$	$t_{stop}(s)$	α_1	α_2	s	$t_{pk}(s)$	χ^2/dof
GRB 060605	73	6317	$0.40^{+0.13}_{-0.09}$	-1.02 ± 0.05	$3.4^{+2.2}_{-1.3}$	484 ± 40	1.3
GRB 060729						96^a	
	218	3016	> 0.8	$-0.21^{+0.04}_{-0.09}$	4.3^b	485^{+97}_{-39}	1.2
GRB 060904b	29.8	120	> 0.2	< -0.8	2.7^b	53^{+11}_{-8}	0.04
	217	1485	$1.7^{+2.0}_{-0.7}$	$-1.11^{+0.14}_{-0.20}$	$2.4^{+4.2}_{-1.7}$	453^{+30}_{-15}	1.5
GRB 061007	29.7	554	27.4 ± 0.4	-1.60 ± 0.01	< 0.02	71.1 ± 30	47^c
GRB 070611	779	8867	$2.0^{+0.7}_{-0.4}$	-0.61 ± 0.14	> 5	2296 ± 151	0.976

Notes.
[a] There is insufficient coverage around the time of the short-duration flare to perform a fit.
[b] s is unconstrained within the range $0.01 < s < 50$.
[c] This model is not a good fit to the early data; see the text for details.

7.1. Calculating the Optical Peak Time

We have calculated the time of the optical peak, t_{pk}, from the early ROTSE-III data for each of the bursts in this paper. For seven of the bursts, the afterglow was already fading at the initial ROTSE-III observation, and thus we only have an upper limit on the time of the optical peak. For the afterglows for which we observe the optical rise, we have fit a smoothly broken power law of the form in Equation 1. When $s > 0$ then this function can fit the light curve peak. We can then calculate the peak time t_p:

$$t_p = t_b \left(\frac{-\alpha_1}{\alpha_2} \right)^{1/[s(\alpha_1 - \alpha_2)]}. \qquad (4)$$

When performing the fits, we allow all parameters to float, including the smoothing parameter, with the constraint that $0.01 < s < 50$. For the afterglows where s could not be constrained, our error bars are essentially marginalized over all values of s. Unlike in the case with the power-law fits in the decaying phase of the afterglow (see Section 6.1), we can fit for s due to the increased leverage in the rising and fading afterglow. Furthermore, we note that we only perform the fit for a suitable time interval around the peak of the burst, to limit the contamination from later light curve breaks.

The results of the fits are shown in Table 8. For two of the afterglows, GRB 060729 and GRB 060904b, there appear to be two optical peaks, and we have listed both peak times in the table. With GRB 060729 (see Figure 3), there is an initial optical flare which may be correlated with one of the peaks in the prompt γ-ray emission; the smooth shape of the latter light curve peak at $t_{pk} = 485$ s is more suggestive of the onset of the forward external shock. With GRB 060904b (see Figure 3), there appears to be two optical peaks, although neither is correlated with the high-energy emission. The smooth profile of the later peak is more suggestive of the onset of the forward shock. For all the bursts, in addition to the question of which optical peak is the onset of the external shock, there may be an ambiguity of what is the proper time to use for the start time, t_0. This issue is discussed below.

Special attention must be paid to the early afterglow of GRB 061007, as our simple model is a poor fit. There is a significant structure in the early afterglow, with two subpeaks at ~60 s and ~100s. Furthermore, the initial optical decline is not quite a power law, with substructure that is visible due to the relatively high-precision photometry made possible by the brightness of the afterglow. Although the model, which traces out the overall shape, suggests that the afterglow has a peak time of 71 s, we

Table 9
Optical Rise Times and Implied Γ_0

GRB	z	$t_{pk}/(1+z)$ (s)	$T_{90}/(1+z)$ (s)	E_{iso} (10^{52} erg s^{-1})	Γ_O $\times (\eta_{0.2} n_0)^{-1/8}$
GRB 050319	3.24	< 39	36	$4.6^{+6.5}_{-0.6}$	$\gtrsim 400$
GRB 050401	2.9	< 9	8.5	32^{+26}_{-7}	$\gtrsim 900$
GRB 050525a	0.61	< 253	5.7	$2.04^{+0.11}_{-0.09}$	$\gtrsim 180$
GRB 050801	1.6	< 9	7.5	$0.22^{+0.36}_{-0.03}$	$\gtrsim 500$
GRB 050922c	2.2	< 55	1.4	$3.9^{+2.7}_{-0.8}$	$\gtrsim 350$
GRB 051109a	2.35	< 11	11.1	$2.3^{+2.4}_{-0.5}$	$\gtrsim 600$
GRB 060111b	~1.0	$\lesssim 18$	~29	$2.9^{+5.2}_{-1.3}$	$\gtrsim 500$
GRB 060605	3.8	101 ± 8	16.5	$2.5^{+3.1}_{-0.6}$	~260
GRB 060729	0.54	~62	75	$0.33^{+0.29}_{-0.06}$	~250
		318^{+60}_{-27}		$0.33^{+0.29}_{-0.06}$	~133
GRB 060904b	0.70	31 ± 6	101	$0.30^{+0.19}_{-0.06}$	~310
		282^{+24}_{-15}		$0.30^{+0.19}_{-0.06}$	~140
GRB 061007	1.26	31 ± 15	33	140^{+110}_{-60}	~680
GRB 070611	2.04	755 ± 50	4	0.34 ± 0.06	~100

also consider the two observations with maximum brightness to be valid peaks. Therefore, we have added a systematic error of ± 30 s to the quoted peak time.

7.2. Estimating Γ_0

Under the assumption that the thin shell model approximations are valid, we can now estimate the initial bulk Lorentz factors for the GRBs. These are tabulated in Table 9. For the bursts where the initial ROTSE observation was obtained after the afterglow was already fading, we obtain a lower limit in the bulk Lorentz factor. For the remaining bursts, we see a large range in initial Lorentz factors, ranging from relatively slow jets in bursts such as GRB 070611 ($\Gamma_0 \sim 100$) to highly ultrarelativistic jets in burst such as GRB 050401 ($\Gamma_0 \gtrsim 900$). This latter burst is notable in that it has the largest E_{iso} in the set, combined with one of the most rapid implied optical rise times, after correcting for cosmological time dilation. In combination, this implies a very fast jet. We also note that in no case is the initial bulk Lorentz factor estimated to be smaller than $\Gamma_0 \sim 100$, which has been estimated as the minimum for which the γ-ray production is possible (Piran 2005).

At this stage, it is worth exploring the validity of our assumptions for calculating the initial Lorentz factor, especially as it applies to individual bursts. These include that the optical afterglow traces the forward external shock, the validity of the thin shell approximation, and that we have used the proper start time, t_0.

We first address the assumption that the optical afterglow traces the forward external shock. As we have shown previously, the broadband early afterglow spectra are all consistent with forward shock emission, with the notable exception of the X-ray flares. The optical afterglow appears to be less contaminated by prompt (internal shock) emission than the X-ray afterglow, and thus is a better tracer of the forward shock. However, the unfiltered ROTSE-III observations cannot constrain the color evolution in the early afterglow; in other afterglows detected by multi-band instruments, this color evolution appears to be modest or absent, consistent with the external shock hypothesis (Yost et al. 2006; Molinari et al. 2007; Perley et al. 2008). It is not possible to make any definitive statements about color evolution with our present ROTSE-III data set, and therefore we cannot rule out the possibility that the early afterglow does not have a significant reverse shock component. In addition, there are two afterglows, GRB 060729 and GRB 060904b, for which there appear to be two optical peaks. In each case there is a short-duration peak contemporaneous with the γ-ray emission, and a smoother peak after the end of the γ-ray emission. Thus, it seems reasonable to assume the latter optical peak traces the onset of the forward shock.

For the afterglows in which we detect the early rise, we can also check if the power-law index of the rise is consistent with predictions. As the forward shock expands into a homogeneous ISM medium, the afterglow is expected to rise as $f_{\nu,\mathrm{O}} \propto t^2$ (Panaitescu & Vestrand 2008). This is roughly consistent with the onset index of GRB 070611 ($\alpha = 2.1 \pm 0.6$). However, the rise of GRB 060605 ($\alpha = 1.18 \pm 0.33$) and GRB 060729 ($\alpha = 0.9^{+0.7}_{-0.5}$) are shallower, and GRB 061007 ($\alpha \sim 9$) is significantly steeper. As with the afterglow decay, we find a large range of temporal indices, with a large scatter around the predicted value. Here, our conclusions are the same as reported at the end of Section 6.2. Since the broadband spectra are consistent with the onset of the forward shock, we attribute the large scatter in the temporal decay indices to the current simplicity of our model.

We next address the validity of the thin shell approximation. As shown in Table 9, in all the cases except for GRB 060111b and GRB 061007 the optical peak comes after the end of significant γ-ray emission as measured by T_{90}. Therefore, for the majority of bursts, and especially those with very short durations ($T_{90}/z \sim 2$ s) the thin shell approximation should be valid. GRB 061007 requires careful attention. For this burst, the optical peak occurs soon after the end of the main γ-ray emission. Thus, the modeling of this afterglow is certainly more complicated, as demonstrated by the structure in the optical light curve near its peak. Due to the very smooth evolution of the later afterglow, which is consistent with the forward shock, we can infer that the broad outline of the optical peak traces the onset of the forward shock, perhaps with additional contribution from prompt emission near the optical peak. For GRB 060111b, we do not have sufficient ROTSE-III coverage to fully constrain the light curve evolution. It is apparent that the optical peak occurs prior to the second BAT peak (see Figure 2), implying that the thin shell approximation may not be valid in this case.

Finally, we note that these calculations are sensitive to the calculation of the start time of the burst, t_0. As we have noted in Section 3.2, the quoted values of t_0, defined as the first detection of BAT emission with S/N > 6, have a typical error of ± 5 s. This may be significant, especially for the afterglows with the earliest limits, such as GRB 050801. After correcting for cosmological time dilation, even this relatively large uncertainty implies an uncertainty in Γ_0 of less than 10%. More problematic are γ-ray precursors that may not have been detected by BAT due to coverage or sensitivity. A particular cautionary tale is GRB 050319. The original analysis of early optical data showed a shallow light curve break, when using the BAT trigger time Woźniak et al. (2005). Further analysis of BAT slew data demonstrated that the main GRB event was in fact 137 s prior to the original BAT trigger time (Chincarini et al. 2005). As discussed in Quimby et al. (2006), using a grossly incorrect t_0 can create spurious breaks in the afterglow light curve, especially at small $t/\delta t$. Similarly, an incorrect calculation of t_0 will bias the estimation of the bulk Lorentz factor Γ_0. Although we do not know of any other bursts in this paper that had additional episodes of γ-ray emission bright enough to be detected by BAT, we of course cannot rule out the possibility that t_0 is not correct.

8. DISCUSSION

The ROTSE-III telescope network has a unique combination of response time, aperture, and global coverage to trace the evolution of optical afterglows from the earliest time. By combining ROTSE-III observations with the rapid response capabilities of the *Swift* telescope, we can track the earliest phases of the prompt optical emission and afterglow as soon as 10 s after the start of the burst, and follow the afterglow for many orders of magnitude in time. In this paper, we have assembled a complete set of 12 ROTSE-III afterglow light curves observed between 2005 March and 2007 June with a significant number of early optical observations and simultaneous coverage with XRT. With a median response time of 45 s from the start of γ-ray emission (8 s after the GCN notice time), we have the opportunity for a unique look at the onset of the afterglow emission.

This paper has attempted to focus on the commonalities among the set of 12 afterglows, rather than the differences. By analogy, we wish to determine the "climate" of GRB afterglows, rather than simply looking at the "weather." In general, we have a picture where the optical emission traces the forward shock. During the γ-ray emission, some afterglows show additional components. After the early time, the X-ray emission also appears to trace the forward shock, but it is much more contaminated by prompt emission and flaring, both of which can be attributed to activity of the central engine. After excluding X-ray flares, both the X-ray spectral index, β_{X}, and the broadband optical-to-X-ray spectral index, β_{OX}, are consistent with the fireball model predictions for the forward shock. Thus, the optical and X-ray emission are from the same emission region. In almost all cases, $\beta_{\mathrm{X}} \sim -1$ is a good description of the X-ray spectrum, and, after correcting for extinction, the optical emission is consistent with a simple extrapolation of the X-ray spectrum, or with the synchrotron cooling break, ν_c, between the optical and X-ray regime.

While the spectral indices are consistent across afterglows, and consistent with the predictions of the fireball model, the decay indices are not. We have found the afterglows that fade rapidly in the optical also fade rapidly in the X-rays. The very slowly decaying GRB 060729 (Figure 3) and the rapidly decaying GRB 061007 (Figure 3) are very different temporally, yet have very similar spectral features, as illustrated in Figure 4. In the case of the slowly decaying afterglows, we can posit some form of long-duration energy injection from the central engine to re-energize the blast wave while leaving the synchrotron

spectrum unchanged, but this is somewhat ad hoc, and does not explain the break times (Panaitescu et al. 2006; Fan & Piran 2006). In addition, energy injection cannot explain the rapidly decaying afterglows such as GRB 061007 and GRB 050525a. Melandri et al. (2008) also noted that several afterglows are not consistent with the fireball model, even after accounting for energy injection. Although the absolute value of the decay index is incorrectly predicted by the fireball model, the relative decay indices between the optical and X-rays is roughly consistent with the predictions for a forward shock expanding into a constant density medium. That is, for most afterglows, the optical decay is slightly shallower than the X-ray decay or is consistent with the same synchrotron regime. The failure of the fireball model to correctly predict the absolute value of the decay index, in light of the remarkably consistent X-ray and broadband spectra, remains the fundamental limitation of the model.

Willingale et al. (2007) have suggested a model in which the X-ray afterglow can be described as a simple combination of a rapidly decaying prompt component and the rise and fall of the forward shock. In broad strokes, this is consistent with what we observe for most ROTSE-III afterglows. Notably, the X-ray afterglow of GRB 060605 (Figure 2) appears to a superposition of the tail of the prompt emission and the optical afterglow, which traces the onset of the forward shock. Although this superposition model is able to explain the flat portion of the X-ray afterglow without positing long-duration energy injection, we observe a relatively steep optical and X-ray decay that is significantly more rapid than predicted by using the X-ray spectral index and standard fireball parameters. Conversely, the extraordinarily long-lived shallow decay of the afterglow of GRB 060729 also cannot be described by this simple superposition model. Thus, for many of the afterglows there remains an inconsistency between the spectral and temporal properties.

In this paper, we studied the relation between the early optical and X-ray afterglow, focusing on the onset of the forward shock. Yost et al. (2007a) studied the correlation (or lack thereof) between the prompt optical and γ-ray emission for these and other ROTSE-III bursts. They found that there is no obvious correlation between the contemporaneous optical and γ-ray emission at the earliest times. As is the case with the optical and X-ray comparisons in this paper, the vast majority of prompt optical detections and limits are significantly dimmer than an extrapolation of the γ-ray spectrum to the optical regime. However, before the onset of the forward shock, a small subset of prompt optical detections show excess emission. GRB 990123 (Akerlof et al. 1999; Briggs et al. 1999), GRB 050820a (Vestrand et al. 2006), GRB 051111 (Yost et al. 2007a, 2007b), GRB 061126 (Perley et al. 2008), and the "naked-eye burst" GRB 080319 (Racusin et al. 2008) all had optical flashes with flux significantly in excess of an extrapolation of the contemporaneous γ-ray emission. In some cases (e.g., GRB 050820a, GRB 080319), the optical flux was correlated with the γ-ray flux, and in other cases (e.g., GRB 990123), they were not correlated. The excess optical component may be from a different emission region (e.g., large-angle emission; Panaitescu & Kumar 2007; Kumar & Panaitescu 2008), or it may be dominated by a different emission process such as the synchrotron-self-Compton mechanism (e.g., Wei 2007; Kumar & Panaitescu 2008).

For the 12 ROTSE-III bursts presented in this paper, none of the prompt optical detections are obviously correlated with the prompt γ-ray emission. For example, optical afterglow of

GRB 060111b has maximum flux prior to the second γ-ray peak, and does not appear to be correlated. On the other hand, the single bright observation of GRB 060729 may coincide with one of the γ-ray peaks, but not the other. This was an exceptionally luminous GRB, and the optical emission is significantly dimmer than an extrapolation of the γ-ray spectrum. Due to happenstance, none of the exceptionally bright optical afterglows has been observed by ROTSE-III and XRT. Instead, the present prompt detections are more akin to GRB 061121 (Page et al. 2007) and XRF 071031 (Krühler et al. 2009). In the case of GRB 061121, the second γ-ray peak is observed in the X-rays, NUV, and ROTSE-III band. Notably, the peak is very blue, and although the peak is prominent in the NUV, it is not significantly observed in the C_R filter. Similarly, the high-precision photometry of the late afterglow of XRT 071031 shows that X-ray flares may be visible in the optical, although they are also very blue in color. Thus, the red sensitivity of ROTSE-III may make it more difficult to see the contribution from the prompt emission except for the most luminous optical flashes.

After the onset of self-similar evolution in the forward shock, we can use the peak time of the forward shock to estimate the initial bulk Lorentz factor of the outflow, Γ_0. Through a broadband spectral analysis we have shown that the optical afterglow is a relatively clean tracer of the forward external shock, and thus we can use the optical peak time to estimate Γ_0. For the 12 bursts in this paper, this covers a wide range, from $\sim$100 for the low-luminosity, late peaking GRB 070611, to $\gtrsim$900 for the high-luminosity, early peaking GRB 050401. For no bursts do we estimate $\Gamma_0 < 100$, which has been estimated as the minimum for which the creation of a non-thermal GRB spectrum is possible (Piran 2005). The range of Lorentz factors is consistent with that observed in other GRBs (e.g., Soderberg & Ramirez-Ruiz 2002; Molinari et al. 2007). Although we have shown that the fireball model is inadequate in predicting the absolute value of the temporal indices of the early afterglow, the time of the onset and the implied Γ_0 are both consistent with predictions (e.g., Piran 2005; Guetta et al. 2001).

The *Swift* satellite has opened a new era of GRB observations, allowing prompt and early multi-wavelength observations of a large sample of bursts and afterglows. By combining rapid GRB observations with the ROTSE-III telescope network with XRT coverage, we have been able to peer into the fireball and constrain the initial bulk Lorentz factor for a large number of GRBs. Although afterglows show common X-ray and broadband spectral properties that are consistent with the predictions of the fireball model, the temporal properties are quite different. It is not yet clear if a single model will be able to explain the "weather" that determines the large variety of temporal decay indices.

REFERENCES

Akerlof, C., et al. 1999, Nature, 398, 400
Akerlof, C. W., et al. 2003, PASP, 115, 132
Arnaud, K. A. 1996, in ASP Conf. Ser. 101, Astronomical Data Analysis Software and Systems V, ed. G. H. Jacoby & J. Barnes (San Francisco, CA: ASP), 17
Band, D., et al. 1993, ApJ, 413, 281
Band, D., et al. 2005, GCN Circ., 3466
Barthelmy, S. D., et al. 2005, Space Sci. Rev., 120, 143
Bertin, E., & Arnouts, S. 1996, A&AS, 117, 393
Briggs, M. S., et al. 1999, ApJ, 524, 82
Burrows, D. N., et al. 2005, Science, 309, 1833
Burrows, D. N., et al. 2007, RSPTA, 365, 1213
Butler, N. R., & Kocevski, D. 2007, ApJ, 663, 407
Butler, N. R., Kocevski, D., Bloom, J. S., & Curtis, J. L. 2007, ApJ, 671, 656
Chen, S. L., Li, A., & Wei, D. M. 2006, ApJ, 647, L13
Chincarini, G., et al. 2005, arXiv:astro-ph/0506453
Corsi, A., et al. 2005, A&A, 438, 829
de Pasquale, M., et al. 2006, MNRAS, 365, 1031
de Pasquale, M., et al. 2007, MNRAS, 377, 1638
D'Elia, V., et al. 2005, GCN Circ., 4044
Dickey, J. M., & Lockman, F. J. 1990, ARA&A, 28, 215
Fan, Y., & Piran, T. 2006, MNRAS, 369, 197
Fan, Y. Z., & Wei, D. M. 2005, MNRAS, 364, L42
Foley, R. J., Chen, H.., Bloom, J., & Prochaska, J. X. 2005, GCN Circ., 3483
Fox, D. W., et al. 2003, Nature, 422, 284
Fugazza, D., et al. 2006, GCN Circ., 5513
Fynbo, J. P. U., Hjorth, J., Jensen, B. L., Jakobsson, P., Moller, P., & Nørønen, J. 2005, GCN Circ., 3136
Gehrels, N., et al. 2004, ApJ, 611, 1005
Gomboc, A., et al. 2009, in AIP Conf. Ser. 1133, Gamma-ray Burst: Sixth Huntsville Symp., ed. C. Meegan, C. Kouveliotou, & N. Gehrels (Melville, NY: AIP), 145
Granot, J., & Sari, R. 2002, ApJ, 568, 820
Grupe, D., et al. 2006a, GCN Circ., 5365
Grupe, D., et al. 2006b, GCN Circ., 5505
Grupe, D., et al. 2007, ApJ, 662, 443
Grupe, D., et al. 2009, arXiv:0903.1258
Guetta, D., Spada, M., & Waxman, E. 2001, ApJ, 557, 399
Hill, J. E., et al. 2004, Proc. SPIE, 5165, 217
Holland, S., et al. 2005, GCN Circ., 3475
Jakobsson, P., Fynbo, J. P. U., Paraficz, D., Telting, J., Jensen, B. L., Hjorth, J., & Cern, J. M. C. 2005, GCN Circ., 4029
Jakobsson, P., Fynbo, J. P. U., Tanvir, N., & Rol, E. 2006, GCN Circ., 5716
Klotz, A., Boer, M., Atteia, J. L., & Gendre, B. 2009, AJ, 137, 4100
Kobayashi, S. 2000, ApJ, 545, 807
Kobayashi, S., & Zhang, B. 2003, ApJ, 582, L75
Krimm, H. A., et al. 2007, ApJ, 665, 554
Krühler, T., et al. 2009, ApJ, 697, 758
Kumar, P., & Panaitescu, A. 2000, ApJ, 541, L51
Kumar, P., & Panaitescu, A. 2008, MNRAS, 391, L19
Lazzati, D., & Perna, R. 2007, MNRAS, 375, L46
Li, Y., Li, A., & Wei, D. M. 2008, ApJ, 678, 1136
Liang, E. W., et al. 2006, ApJ, 646, 351
Maiorano, E., et al. 2005, A&A, 438, 821
Meiksin, A. 2005, MNRAS, 356, 596
Melandri, A., et al. 2008, ApJ, 686, 1209
Meszaros, P. 2006, Rep. Prog. Phys., 69, 2259
Meszaros, P., & Rees, M. J. 1997, ApJ, 476, 232
Molinari, E., et al. 2007, A&A, 469, L13
Morrison, R., & McCammon, D. 1983, ApJ, 270, 119
Norris, J., et al. 2005, GCN Circ., 4013
Nousek, J. A., et al. 2006, ApJ, 642, 389
Osip, D., Chen, H.., & Prochaska, J. X. 2006, GCN Circ., 5715
Page, K. L., et al. 2007, ApJ, 663, 1125
Page, M. J., et al. 2006, GCN Circ., 5221

Panaitescu, A., & Kumar, P. 2007, MNRAS, 376, 1065
Panaitescu, A., Mészáros, P., Burrows, D., Nousek, J., Gehrels, N., O'Brien, P., & Willingale, R. 2006, MNRAS, 369, 2059
Panaitescu, A., & Vestrand, W. T. 2008, MNRAS, 387, 497
Perley, D. A., et al. 2008, ApJ, 672, 449
Perri, M., et al. 2006, GCN Circ., 4487
Peterson, B., & Schmidt, B. 2006, GCN Circ., 5223
Piran, T. 2005, Rev. Mod. Phys., 76, 1143
Piranomonte, S., et al. 2005, GCN Circ., 4032
Quimby, R., Fox, D., Hoeflich, P., Roman, B., & Wheeler, J. C. 2005, GCN Circ., 4221
Quimby, R. M., et al. 2006, ApJ, 640, 402
Racusin, J. L., et al. 2008, Nature, 455, 183
Racusin, J. L., et al. 2009, ApJ, 698, 43
Romano, P., et al. 2006, A&A, 456, 917
Ruiz-Velasco, A. E., et al. 2007, ApJ, 669, 1
Rykoff, E. S. 2005, PhD thesis, Univ. of Michigan
Rykoff, E. S., Miller, J. M., Steeghs, D., & Torres, M. A. P. 2007a, ApJ, 666, 1129
Rykoff, E. S., & Rujopakarn, W. 2006, GCN Circ., 5706
Rykoff, E. S., Rujopakarn, W., & Yuan, F. 2006a, GCN Circ., 5504
Rykoff, E. S., & Schaefer, B. E. 2006, GCN Circ., 5220
Rykoff, E. S., Yost, S. A., & Rujopakarn, W. 2005a, GCN Circ., 4011
Rykoff, E. S., Yost, S. A., & Swan, H. 2005b, GCN Circ., 3465
Rykoff, E. S., Yuan, F., & Yost, S. A. 2007b, GCN Circ., 6497
Rykoff, E. S., et al. 2004, ApJ, 601, 1013
Rykoff, E. S., et al. 2005c, ApJ, 631, L121
Rykoff, E. S., et al. 2006b, ApJ, 638, L5
Sakamoto, T., et al. 2008, ApJS, 175, 179
Sari, R., & Piran, T. 1999a, ApJ, 517, L109
Sari, R., & Piran, T. 1999b, ApJ, 520, 641
Savaglio, S., Palazzi, E., Ferrero, P., & Klose, S. 2007, GCN Circ., 6166
Schady, P., et al. 2006, GCN Circ., 5707
Schady, P., et al. 2007, MNRAS, 380, 1041
Schady, P., et al. 2008, in AIP Conf. Ser. 1000, Gamma-ray Bursts 2007: Proc. of the Santa Fe Conf., ed. M. Galassi, D. Palmer, & E. Fenimore (Melville, NY: AIP), 505
Schaefer, B. E., Rykoff, E. S., Smith, D. A., & Quimby, R. 2006, GCN Circ., 5222
Schlegel, D. J., Finkbeiner, D. P., & Davis, M. 1998, ApJ, 500, 525
Smith, D. A., et al. 2003, ApJ, 596, L151
Soderberg, A. M., & Ramirez-Ruiz, E. 2002, MNRAS, 330, L24
Stetson, P. B. 1987, PASP, 99, 191
Still, M., et al. 2006, GCN Circ., 5226
Stroh, M. C., et al. 2007a, GCN Circ., 6494
Stroh, M. C., et al. 2007b, GCN Circ., 63.3
Thoene, C. C., Jakobsson, P., Fynbo, J. P. U., Malesani, D., Hjorth, J., & Vreeswijk, P. M. 2007, GCN Circ., 6499
Thoene, C. C., Levan, A., Jakobsson, P., Rol, E., Gorosabel, J., Jensen, B. L., Hjorth, J., & Vreeswijk, P. 2006, GCN Circ., 5373
Vanderspek, R., Villaseñor, J., Doty, J., Jernigan, J. G., Levine, A., Monnelly, G., & Ricker, G. R. 1999, A&AS, 138, 565
Vestrand, W. T., et al. 2004, Astron. Nachr., 325, 549
Vestrand, W. T., et al. 2005, Nature, 435, 178
Vestrand, W. T., et al. 2006, Nature, 442, 172
Watson, D., et al. 2006, ApJ, 652, 1011
Wei, D. M. 2007, MNRAS, 374, 525
Willingale, R., et al. 2007, ApJ, 662, 1093
Woźniak, P. R., Vestrand, W. T., Wren, J. A., White, R. R., Evans, S. M., & Casperson, D. 2005, ApJ, 627, L13
Yost, S. A., et al. 2006, ApJ, 636, 959
Yost, S. A., et al. 2007a, ApJ, 669, 1107
Yost, S. A., et al. 2007b, ApJ, 657, 925
Zerbi, R. M., et al. 2001, Astron. Nachr., 322, 275
Zhang, B., Fan, Y. Z., Dyks, J., Kobayashi, S., Mészáros, P., Burrows, D. N., Nousek, J. A., & Gehrels, N. 2006, ApJ, 642, 354
Zhang, B.-B., Liang, E.-W., & Zhang, B. 2007, ApJ, 666, 1002